The Meteoritical Society

Meteoritics & Planetary Science 42, Nr 9, 1627–1646 (2007)
Abstract available online at http://meteoritics.org

Meteorite 3-D synchrotron microtomography: Methods and applications

Denton S. EBEL[1*] and Mark L. RIVERS[2]

[1]Department of Earth and Planetary Science, American Museum of Natural History, Central Park West at 79th Street, New York, New York 10024, USA
[2]Consortium for Advanced Radiation Sources and Department of the Geophysical Sciences, The University of Chicago, 5640 South Ellis Avenue, Chicago, Illinois 60637, USA
[*]Corresponding author. E-mail: debel@amnh.org

(Received 12 January 2006; revision accepted 19 April 2007)

Abstract–Methods of synchrotron X-ray computed microtomography (XRCMT) are described, which allow nondestructive, high spatial and contrast resolution imaging of the density structures of meteorites and their components in three dimensions. Images of bulk chondrites (to one cubic centimeter in size) reveal compound chondrules, chondrule/matrix volumetric ratios, metal and sulfide distribution, petrofabrics, and 3-D chondrule and calcium-aluminum inclusion (CAI) sizes and shapes. Images of separated chondrules and CAIs reveal void spaces, mineral intergrowth textures, and the true locations of crystal rims and cores, at resolutions to <8 cubic micron/volume element. Images of achondrites reveal mineral fabrics and crystal zoning. Lunar glass spherules can be searched for phenocrysts bearing deeply sourced melt inclusions. A companion DVD and URL contain images for classroom and research use. Numerical techniques for quantification of X-ray computed microtomography (XRCMT) data and its potential applications are discussed. Three-dimensional X-ray images of meteorites provide a way to discover components of interest and to precisely slice samples to expose these components with minimal damage and loss of material. Three-dimensional studies of petrographic features (size, shape, texture, and modal abundance) of chondrites and their components, as well as other meteorites, have definite advantages over standard 2-D studies using randomly sliced thin sections.

INTRODUCTION

In 2-D imaging, resolution is described by the size of each picture element, or pixel. Familiar examples are the X-ray maps obtained using the electron microprobe (EMP), in which each pixel has an associated single-valued X-ray emission intensity. In 3-D, a "voxel" is a volume element. Synchrotron X-ray computed microtomography (XRCMT) is a rapid, nondestructive method of producing 3-D images of the interiors of opaque samples (e.g., rocks). Every voxel has an associated single numerical value of the computed X-ray attenuation due to the material in that voxel. In all cases described here, voxels are cubes, and spatial resolution is described by the length of voxel edges in micrometers (μm), which correspond to the edges of square pixels in successive equally spaced slices through the volume. We used XRCMT to record the 3-D density structures of bulk meteorites (0.5–3.0 cm^3) at resolutions of 10–17 μm/voxel edge, and of individual chondrules and calcium-aluminum inclusions (CAIs) at resolutions as fine as 1.2 μm/voxel edge. These results offer a new way to qualitatively assess meteorite textures.

Quantitative results were extracted from subsets of the tomographic data using combinations of commercially available and customized image processing software. Following tomographic analysis, some samples were serially sectioned while others were cut to directly reveal selected interior slices of objects of interest. Conventional optical and electron, ion, or laser microbeam techniques were applied to the resulting 2-D surfaces to augment and validate the 3-D XRCMT data.

We have previously reported preliminary studies using XRCMT (e.g., Weisberg et al. 2002; Hertz et al. 2003; Murray et al. 2003; Schoenbeck and Ebel 2003; Ebel et al. 2004; Ebel et al. 2005; Hylton et al. 2005; Ebel and Rivers 2005). Here we describe these methods and present results of tomographic imaging of ordinary (e.g., Semarkona LL3.0) and carbonaceous (e.g., Allende CV3ox; Al Rais, Acfer 139, and Renazzo CR2) chondrites, and for separated chondrules and CAIs. A DVD containing raw tomographic data, stacks of

consecutive tomographic images through objects, and compilations of those stacks into movies accompanies this paper and is included in this issue. We have found these images to be engaging and informative in teaching educators, students, and the public about meteorites.

SYNCHROTRON X-RAY MICROTOMOGRAPHY

XRCMT is the determination of the 3-D density structure of a solid object by computer-assisted reconstruction based on a series of snapshots of the object in X-ray illumination (Hounsfield 1980; Flannery et al. 1987). The richest literature is in the field of medical diagnostic computer-aided tomography, or CAT scanning, where low energies are sufficient to penetrate samples (e.g., Newton and Potts 1981; Seeram 2001). Higher energies are used in industrial applications, and these techniques have been adapted to fields such as paleontology, soil science, and the permeability and porosity of reservoir rocks (e.g., Mees et al. 2003; van Geet and Swennen 2001; Maissey 2005; Ketcham and Iturrino 2005). Arnold et al. (1983) located CAIs in two Allende specimens (459 and 586 g) at ~1 mm spatial resolution. Heymann et al. (1985) found cm-scale heterogeneity in Allende using X-radiography on sequential slabs. Kondo et al. (1997) examined textures in Moorabie (L3) and Allende and identified void spaces in Allende chondrules. Tsuchiyama et al. (1999) studied an 8 × 8 × 12 mm sample of the Martian meteorite ALH 84001 at two commercial X-ray scanning facilities in Japan, with voxels 9 × 9 ×15 μm and 16 × 16 × 50 μm. They were able to distinguish plagioclase-normative glass, orthopyroxene, cracks, chromite, and other features with a spatial resolution of a few tens of μm with the finer resolution instrument. Based on their study of the Kobe (CK4) meteorite, Tsuchiyama et al. (2002) proposed nondestructive curation of rare samples using microtomography. Carpenter and Gillies (2005) investigated metal grain coarsening and metal/sulfide distribution in a large (50 kg) slab of the Mundrabilla iron at 1 mm intervals, and a smaller piece at 0.5 mm intervals, using a CT facility at Kennedy Space Center, Florida. Nanometer-resolution tomographic reconstructions of meteoritic materials from high-resolution transmission electron microscope (TEM) images have been reported by Zega et al. (2006).

The CT facility at the University of Texas is highly productive in earth science and paleontology applications (University of Texas 2007; Carlson and Denison 1992). McCoy and Carlson 1998 (cf. Carlson and McCoy 1998) examined metal segregation in Lodranite samples larger than 8 cm^3, at a voxel size of 140 × 140 × 250 μm. Kuebler et al. (1999) obtained the sizes of irregular metal-troilite grains in samples of the meteorites Bjurböle, Kelly, and Hammond Downs at a resolution of 100 μm per voxel edge. Vesiculation was studied in terrestrial basalts (e.g., Song et al. 2001; Sahagian et al. 2002), asteroidal basalts (McCoy et al. 2002, 2003), and ordinary chondrites (Benedix et al. 2003). Nettles et al. (2003) investigated chondrule melting in experimental charges. Facilities based on medical and industrial technology are well-suited to large samples, but are limited in resolution (Carlson et al. 2003). Recent advances in Fresnel zone plate optics have pushed resolution to <50 μm scales for application to very small objects (Attwood 2006; Nakamura et al. 2007).

The synchrotron produces a very flat wavefront with high energy flux per unit area that is not subject to the energy loss related to the spherical dispersion of a point source. Synchrotron microtomography allows for much finer spatial resolution of density contrasts, but dense samples must be correspondingly smaller to allow X-ray penetration and to capture many pixels in a small field of view. Feng et al. (1999) studied submillimeter deep-sea spherules at the National Synchrotron Light Source at Brookhaven National Laboratory, New York, USA, with cubic voxels 3.6 μm on an edge. Tsuchiyama et al. (2001; cf. Uesugi et al. 2001) described the ability of the new, dedicated synchrotron radiation facility SPring 8 in Japan (SPring8 2007) to obtain 1.5 μm resolution in 0.5 mm samples, although their figures state cubic voxels are 6 μm on an edge. Other studies there include those by Ikeda et al. (2004), Kitamura et al. (2001), Okazawa et al. (2002), and Tsuchiyama et al. (2000, 2005). Topics studied at the Advanced Photon Source at Argonne National Laboratory (Dept. of Energy), Argonne, Illinois, USA, include porosity in meteorites (Flynn et al. 2000), water drainage in soils (Wildenschild et al. 2000, 2001), inclusions in diamonds, and cracks in rocks from nuclear waste repositories. The maximum spatial resolution is about 1 μm per voxel edge, or 0.002 times the size of the sample, whichever is larger. The available X-ray energies allow a wide range of sample sizes and compositions to be examined (Rivers et al. 1999). On ultrasmall samples, it is possible to obtain 3-D elemental maps using synchrotron fluorescence microtomography (Rivers et al. 2001; Flynn et al. 2003; Ikeda et al. 2004; Ignatyev et al. 2007). For low-density samples (e.g., aerogel), lambda tomography can be used to explore cm-scale volumes at a spatial resolution of 2–3 μm (Ebel and Rivers 2005).

Instrument

For this work, tomographic analysis was performed on beamline 13BM-D at the Advanced Photon Source (APS) (Sutton 2006), Argonne National Labs, U.S. Department of Energy, operated by the University of Chicago through the Geology-Soil-Environmental Consortium for Advanced Radiation Sources (GSE-CARS). The bending magnet at APS generates a high-flux, high-brilliance X-ray beam of up to 50 keV. The X-rays are synchrotron radiation produced by 7 GeV electrons orbiting at a constant ~100 mA in the 1104 m circumference storage ring. Current is maintained at 100 mA

in “top-up” mode by constant injection of electrons. The X-ray beam enters each of 70 tangential beamlines through a beryllium window.

Our experimental apparatus for most of the present work is pictured in Fig. 1 and is shown schematically in Fig. 2. On beamline 13BM-D, the beam encounters horizontal and vertical collimating slits, and a double diffracting Si[220] monochromator before passing through the sample. A single-crystal 500 μm yttrium-aluminum garnet (YAG) scintillator is placed 30–100 mm downstream of the sample, followed by a 45° mirror that reflects visible light through a lens or microscope objective onto a high-speed 12-bit charge-coupled device (CCD) camera (Princeton Instruments Pentamax) (Fig. 1). Before August 2005, we used a 5×, 10×, or 20× Mitutoyo microscope objective (Fig. 1), which remains optimal for small fields of view (< ~6 mm). Recently, we found that a Nikon macro lens provides much sharper images for objects with larger fields of view. The CCD has 1317 × 1035 pixels in an 8.98 × 7.04 mm area. Data is typically collected by binning CCD readout by a factor of two in both dimensions, cutting exposure time and data volume by ~4×. A region of interest (ROI) can be defined on a subset of the CCD to minimize readout time. Instrument control and data collection use the EPICS software, coupled with Princeton Instruments’ WinView and the Microsoft COM interface.

The apparatus is configured to allow variation of the distance between the sample and the scintillator-mirror-camera ensemble. A longer distance enhances phase contrast, providing better imaging of boundaries between sample regions with only subtle differences in attenuation. This effect is similar to the Becke line observed in the petrographic microscope.

A single data set is collected by rotating the sample from 0° to 179.5° in 0.5° steps, then rotating again through 180° at 0.5° steps, starting at 0.25° for 720 angles. At each angle, a static image (radiogram) is taken, at an exposure time of 0.2 to 4.0 s. The sample is removed from the beam, usually every 50 or 100 images, and a white field is collected to enable later correction of the data for variations in the beam. Each raw data set is then 738 binary 12-bit 658 × 515 pixel images totaling ~375 KB in size. Alignment of samples for data collection can be time-consuming, but collection itself is rapid. In 2001, collection of a single data set (e.g., Al Rais, DVD Fig. 1) at 0.8 s/exposure took ~45 min. By reducing dwell time, a similar collection in 2005 took ~10 min. Files of raw data and set-up conditions are the basis for all off-line processing, which is described below.

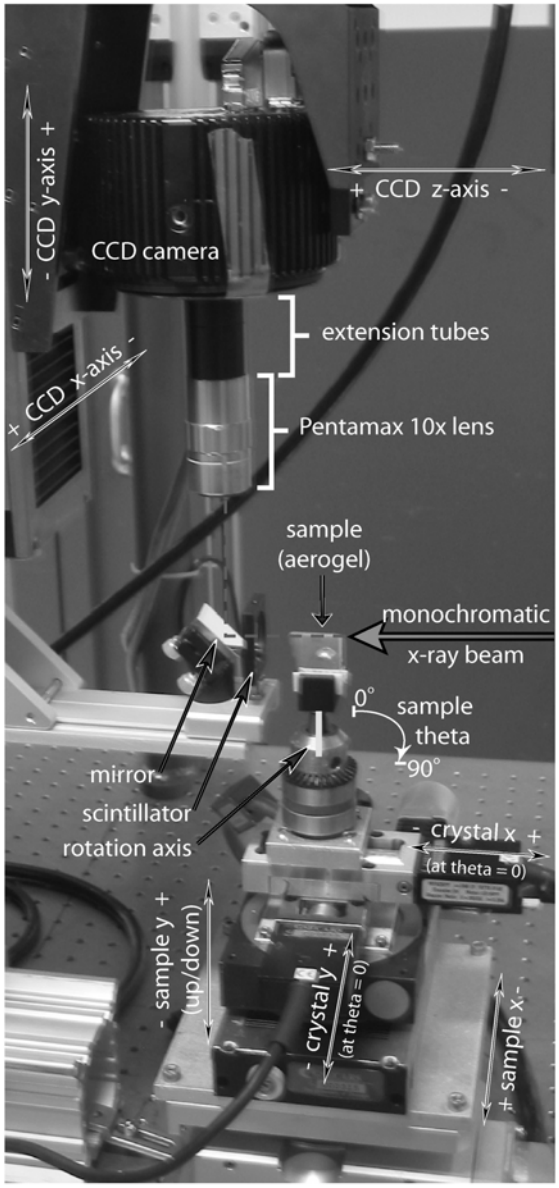

Fig 1. Photo of stage and camera tomography set-up at the beamline.

Sample Handling

These conditions are specific to the apparatus used at APS, but are generally applicable. For dense samples such as meteorites, the sample must be cut so that the widest horizontal cross section direction is narrower than the maximum field of view of the instrument. With the Mitutoyo lens, this was ~11 mm, but the Nikon macro lens used in later work allowed a wider field of view. The sample vertical dimension (z), limited only by stage range, can be up to 40 mm. Minimum spatial resolution is, then, 11 mm/(1300/2) pixel = ~17 μm/pxl. By varying magnification before the CCD, the field of view can be reduced commensurate with the maximum width of smaller samples to obtain higher spatial resolution. Bulk samples are therefore small fragments or are cut to tetragonal prisms due to the difficulty and waste in making perfect cylinders (e.g., Fig. 3). Samples are mounted with a low-density material (tape, epoxy) on the tip of an appropriate rod (toothpick, dowel) that is locked in a drill chuck centered on the

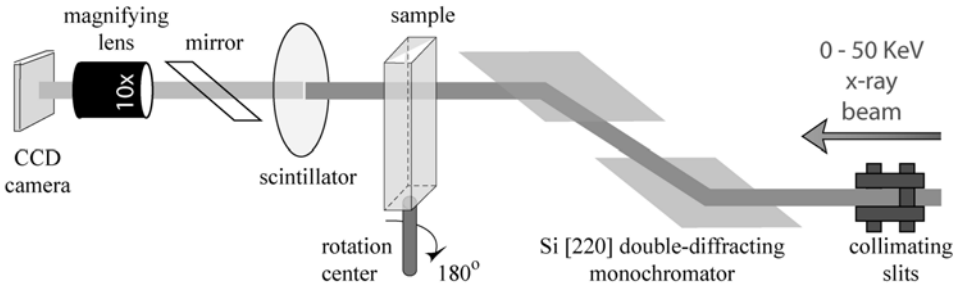

Fig 2. Schematic of light path in synchrotron tomography.

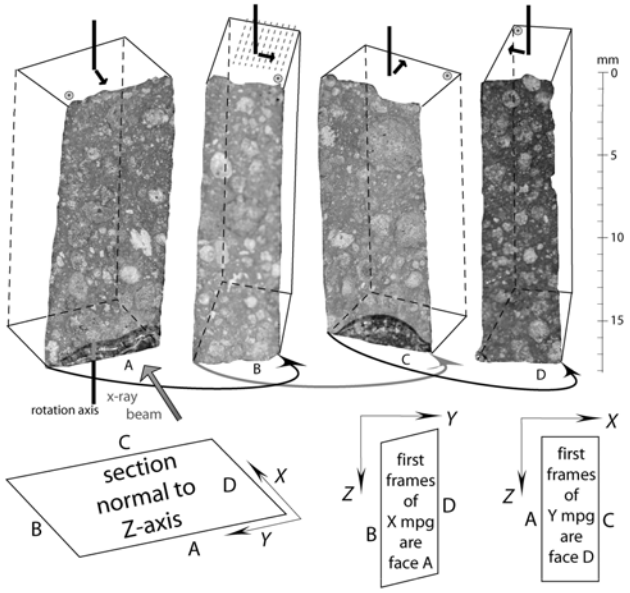

Fig 3. 3-D layout of Allende sample in tomography experiment.

instrument stage (Fig. 1). For a sample with rectangular cross section, it is preferable that a flat face be oriented normal to the beam in order to facilitate postanalysis image handling and to ensure serial sectioning nearly parallel to a set of tomographic image stacks (Fig. 3).

The stage of the instrument is automated for fine x, y, z, and rotational control (Fig. 1). The entire stage assembly sits on a substage, which also has x, y control, on a movable optical table. On many bulk samples, a series of volume analyses was obtained, stacked vertically, by incrementing stage z motion between data collections with a small overlap. That is, a complete raw data set was collected, then the sample was raised, and then subsequent raw data sets collected. After processing (see below), these data were recombined into a single 3-D image of a slender "stick" of material. To collect such stacks without rotating the sample out of the field of view of the instrument requires mounting the sample as close to the vertical as possible on the supporting rod. Sample heating is negligible, as shown by an analysis and tests on organic compounds presented in a subsequent paper.

Reconstruction Algorithm

Raw data is processed to obtain a 3-D array, or volume, with an X-ray attenuation value for each (x, y, z) volume element, or "voxel." The whole volume can be thought of as a stack of virtual, parallel "slices" through the sample. Processing routines are written in C and IDL. First, data is corrected for dark current (signal with no X-rays, plus a digitization offset), and for white field (X-ray signal with no sample). The latter includes effects of nonuniformity in the incident X-ray beam (e.g., scratches in the beryllium window), in the scintillator response, and in the CCD response (e.g., pixel defects). During this correction, each pixel (x, y) of each of 720 images (at angles theta) is converted to a 16-bit integer (scaled to 100,000) for computational efficiency (Rivers 2007). In samples rich in high-attenuation material (metal), attenuation must be scaled to a lower factor (e.g., 50,000, for Itqiy) (DVD Fig. 2).

Next, a Shepp-Logan edge-sharpening filter is applied to sinograms of the data, which are X-projections through the y slices as functions of angle theta, in the logarithm of the ratio of intensity through the sample to the intensity through adjacent air in each frame of the raw data. Ring artifacts are present in the sinograms, in part because higher energy harmonics produced in the incident beam by the monochromator (e.g., Si[440]), and absorbed differently by the sample, impact detector elements in differing ratios because of the same nonuniformities corrected using the white field. These artifacts, however, cannot be corrected using the white field. Ring artifacts show up as rings in virtual slices normal to the sample z axis, and cylindrical "bullet" artifacts in virtual slices parallel to the z axis. In this work, they are suppressed but not eliminated by a row averaging technique. Late in 2005, it was discovered that flat field averaging in the preprocessing step substantially reduces ring artifacts, allowing reprocessing of previous work to produce better results. All results in this paper were reprocessed in 2006. Following preprocessing, selected sinograms are back-projected onto x, and a rotation axis for final back-projection is chosen manually by inspection, followed by final reconstruction of the data set. This process results in a "volume" file, written in the NetCDF format developed at

NCAR (NCAR 2007), in which 16-bit integers describe the density structure for the (x, y, z) of the sample volume. A web tutorial provides further information (Rivers 2007), and reconstruction algorithms and tomographic data-handling software are available (GSECARS 2007).

Output

Even small data sets contain 200–500 MB of density information, so robust computer hardware is required. Reconstructed volumes are handled using routines developed in IDL (RSI 2007). Volumes can be cropped, combined, and rotated as 3-D arrays. Multiple vertically contiguous data sets collected sequentially at several z-positions of one sample are combined into a single volume. Such combined volumes can run over 1 GB, requiring a 64-bit implementation of software. Due to beam intensity differences between the bottom of one volume and top of the next, slight discontinuities are visible between the vertically joined segments of such combined volumes. As noted above, a sample with rectangular cross section (a, b) produces a data set with (x, y) dimensions greater than the diagonal: $(x + y)/2 > (a^2 + b^2)^{1/2}$, because the sample must rotate in the field of view. As much as 50% of the data volume can be the air outside the actual subset representing the sample. Volume files can therefore be reduced significantly in size by cropping in their x and y directions.

From these fully processed volume files, stacks of 2-D images and movies are generated using software written in IDL. For each axis x, y, and z of the sample, the volume file can be output as a stack of sequential images of X-ray attenuation, each image separated from the previous image, or slice, by the voxel edge length (spatial resolution) of the analysis (Fig. 4). Each pixel of such a 2-D map has a grayscale value proportional to the mean X-ray attenuation of the material in the voxel which that pixel represents. These sets of slices can be written as separate, sequential image files, either 8-bit jpeg, 8-bit tiff, or 16-bit tiff. Image stacks can also be combined into movies and output in the standard 8-bit mpeg format. Eight-bit images are limited to 256 grayscales, but are of much smaller size than the 16-bit tiff images that retain the 65,536 grayscales of the original reconstructed volume. The 8- and 16-bit images appear similar to the human eye, particularly given the limited capabilities of computer monitors to display grayscales, but automated routines to obtain information from these stacks benefit from the higher density 16-bit tiff resolution.

To accentuate contrast between different silicate phases, maximum and minimum grayscale values can be set when creating 8-bit image or movie files. Typical values are 0–15,000 for chondrite volumes. Each slice resembles a backscattered electron (BSE) image when rescaled into 256 grayscales. To browse through meteorite volumes slowly, the Image/J software (ImageJ 2007) can be used to import, scroll through, and annotate both 8-bit and 16-bit tiff stacks (File > Import > Image sequence). For other purposes, such as quick surveys of meteorite volumes, movies illustrate the sample as if one were viewing successive planes normal to the sample x, y, or z axis. A disadvantage of movies of large samples is that older mpeg formats cannot support frames with total pixel number >307,200 (640 × 480). In such cases, a zoom of 1/2 (2 × 2 pixel binning) is used, which degrades the spatial resolution of the output. This disadvantage does not apply to tiff image stacks.

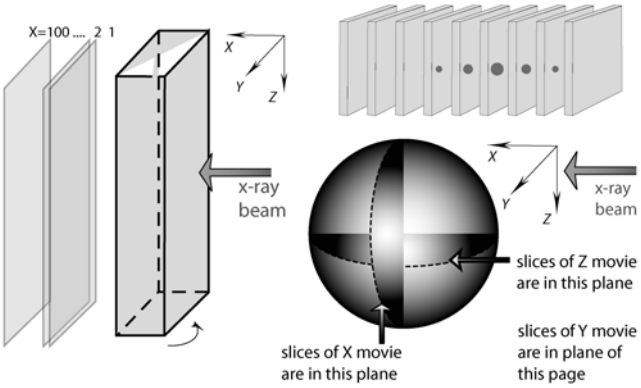

Fig 4. Relation between image labels and sample x, y, and z axes.

X-Ray Attenuation

The observed attenuation values allow an educated estimate of the identities of chondrules, metal/sulfides, CAIs, and other objects in bulk meteorite samples, and of particular crystals in chondrite components. X-ray energies and sample sizes can be chosen to optimize contrast in particular samples. Because X-ray absorption is only linear in density, but goes as the third or fourth power of atomic number (Z), even a small amount of a high atomic number element (Ca, Fe, Sr, etc.) causes large differences in absorption. It is therefore possible to distinguish, for example, spinel ($MgAl_2O_4$) from melilite ($Ca_2Al_2SiO_7$-$Ca_2MgSi_2O_7$) due to their different Ca contents (Fig. 5a; Table 1). Similarly, it should be possible to identify fremdlinge (El Goresy et al. 1978, 1979) in individual CAIs due to the high atomic number of platinum-group elements (PGEs) relative to iron-nickel alloy or sulfide (Fig. 5b). More subtle contrasts such as mesostasis composition gradients (Grossman et al. 2002) or contrast between equilibrated olivine and orthopyroxene are not observable in tomography. Tsuchiyama et al. (2002) discussed the utility of attenuation values to quantify mineralogy in the Kobe meteorite, and reported attenuation or "CT values" for a variety of pure minerals at different conditions on a Nittetsu Elec. Co. micro X-ray CT scanner.

In Table 1, note that at 15 keV the photoabsorption coefficient for melilite is 12.0 and spinel is 4.8, while at 20 keV they are 5.2 and 2.1 keV. More than a factor of two in

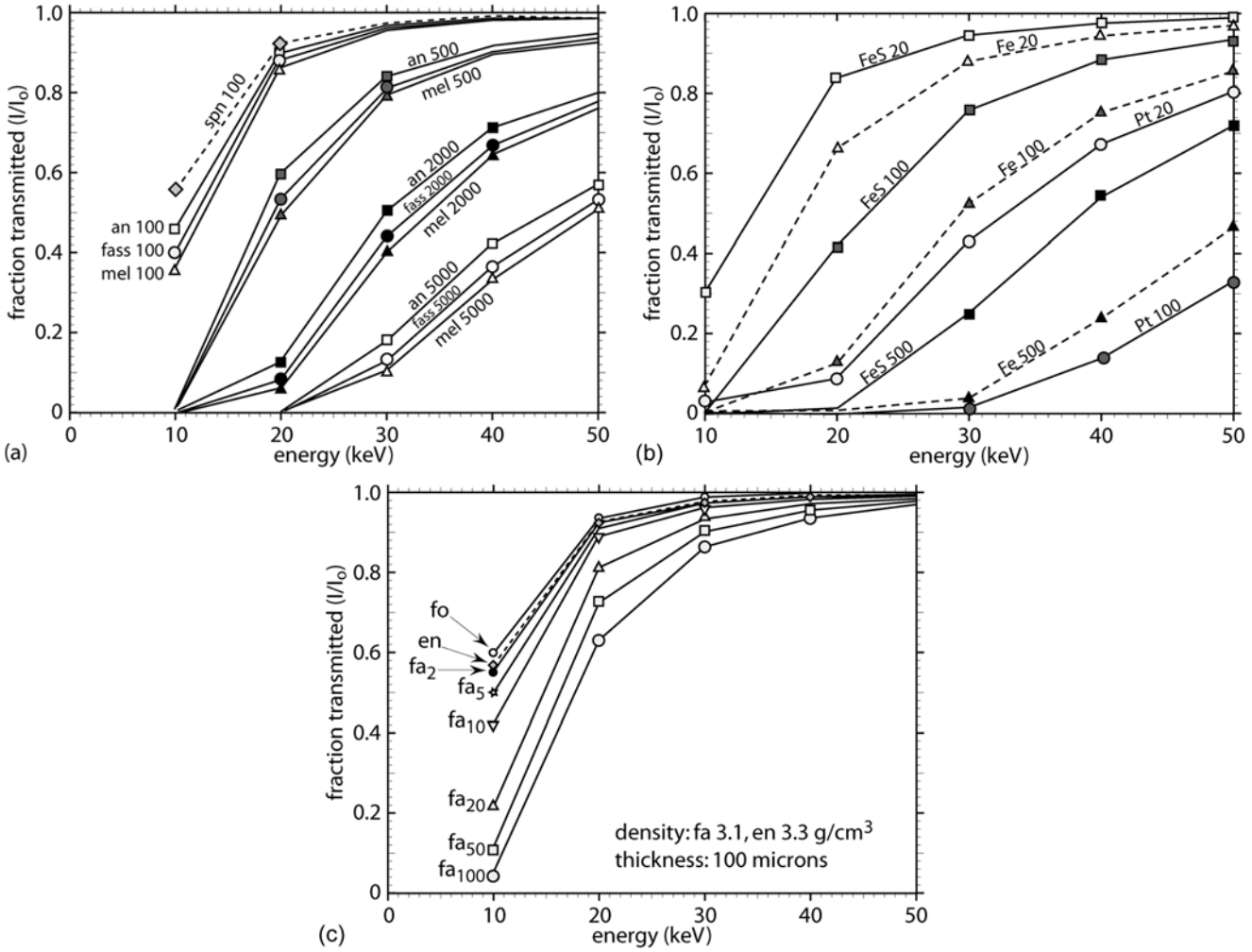

Fig 5. a–c) Energy/contrast relations for (a) CAI minerals, (b) metal and troilite, and (c) Fe-Mg silicates.

contrast is easy to measure. This contrast is almost entirely due to the Ca in melilite, at a much higher *Z* than O, Mg, Al, and Si, which are the other major elements. One thing that helps with contrast is to work at relatively low energy, less than 20 keV. This means that the samples must be small (<4 mm) in cross section to allow X-ray penetration at low energy. However, at low energy, high-attenuation (metallic) grains may cause shadowing of X-rays, causing artifacts in final density maps. The trade-off between X-ray energy and resolution must be made on a sample-by-sample basis. Many CAIs and chondrules are in the 4 mm size range. For larger samples, spatial resolution and contrast suffer because of the larger pixel size and higher energies required, so it is advantageous to cut such samples into smaller pieces.

Relationships between sample size and X-ray attenuation for some common minerals in chondrules and CAIs are illustrated in Fig. 5. Calculations are for monominerallic volumes at given thicknesses. In Fig. 5a, curves are labelled by mineral identity (an = anorthite $CaAl_2Si_2O_8$, density ρ = 2.76 g/cm^3; fass = $CaAl_{0.76}Ti_{0.12}Si_{1.63}O_6$, ρ = 2.76; mel = $Ca_2Mg_{0.4}Al_{1.2}Si_{1.4}O_7$, ρ = 2.7; spn = spinel $MgAl_2O_4$, ρ = 3.6) and sample thickness (100, 500, 2000, and 5000 μm). Figure 5b illustrates platinum metal (ρ = 16) at 20 and 100 μm thicknesses, compared with troilite (FeS, ρ = 4.7) and pure iron (ρ = 8) at 20, 100, and 500 μm thicknesses. Olivine (Mg_2SiO_4-Fe_2SiO_4) with X_{fa} from 0 to 100 (all with ρ = 3.1) is compared with pure enstatite ($MgSiO_3$, ρ = 3.3) for 100 μm sample thickness in Fig. 5c. As the Fe-rich endmember fayalite is added to pure-Mg forsterite, attenuation increases dramatically, but this difference decreases at higher energy for a fixed sample thickness. With increasing sample size, higher energy is required to penetrate a sample. At low energies, the fraction of X-ray energy transmitted (I/I_o) is small, but for small samples, there is higher contrast between minerals. Transmittance increases at higher energies, but attenuation differences between minerals become smaller. For example, to bring out differences in fayalite content of olivine, an energy of 20 keV would be preferred (Fig. 5c), but a sample penetrable by this energy would be about the size of an individual chondrule (2 mm). In

Table 1. Calculation of absorption contrast between melilite and spinel, assuming they have the same density (3.0 gm/cm^3) and thickness (1000 μm). Totals are the absorption cross sections (cm^2/gm) due to photoabsorption, and absorption due to elastic and inelastic scattering at each energy. Characteristic depth is a measure of the sample thickness required to reduce intensity to 1/e = 0.368; 90% absorption occurs at about twice this depth.

Absorption coefficients, typical melilite, $Ca_{2.0}Si_{1.2}Al_{1.6}Mg_{0.2}O_7$ (Srinivasan et al. 2000)						
Energy	Photo	Elastic	Inelastic	Total	Depth (μm)	I/I_o
10 keV	37.97	0.5587	0.1137	38.65	86.25	9.2205E-06
15	11.54	0.3334	0.1343	12.01	277.7	0.0272
20	4.864	0.2222	0.1455	5.232	637.1	0.2081
25	2.469	0.1589	0.1518	2.780	1199	0.4344
30	1.413	0.1194	0.1552	1.687	1976	0.6028
Absorption coefficients for spinel, $Mg_{2.5}Al_5O_{10}$						
Energy	Photo	Elastic	Inelastic	Total	Depth (μm)	I/Io
10 keV	15.64	0.4256	0.1153	16.19	206.0	0.0078
15	4.455	0.2515	0.1361	4.843	688.3	0.2339
20	1.800	0.1668	0.1473	2.114	1577	0.5303
25	0.8859	0.1189	0.1535	1.158	2878	0.7065
30	0.4949	0.0891	0.1567	0.7407	4500	0.8007

tomography of individual chondrules (DVD Fig. 3) and a small sample of the Martian meteorite Zagami (DVD Fig. 4), zoning of Fe in individual olivine and pyroxene crystals is easily observed.

Highly attenuating samples limit application of the technique. For example, the anomalous EH chondrite Itqiy has a metal content, hence sample density, higher than a limit that precludes effective microtomography, in our experience. Itqiy contains equigranular enstatite and 22% metal by volume forming triple junctions, with sulfides in intergranular "corners" (Patzer et al. 2001). From a 0.185 g fragment of Itqiy, two vertically stacked tomographic image sets were obtained at 25 keV and 8.715 μm/voxel spatial resolution. Image stacks and movies were produced from the combined, cropped volume file (DVD Fig. 2) (Ebel 2007). The images were compromised by X-ray attenuation shadows cast by accumulations of metal and sulfide at intergranular corners, and by the fact that the data were collected at a low energy of 25 KeV. Nevertheless, the texture in 3-D corresponds to that reported by Patzer et al. (2001, their Fig. 1); quantitative data could be extracted from these images to describe metal connectivity and wetting.

Image Analysis

Synchrotron microtomography is a new way to observe how the components of the various meteorites are put together. The DVD-ROM included in this issue contains a selection of image sets and movies for chondrites of particular interest. Although the eye and brain make sense of these movies, translating human sensory algorithms into image analysis codes that can extract quantitative information from these images is quite difficult (e.g., Song et al. 2001; Proussevitch and Sahagian 2001). Frame-by-frame quantitative analysis of the 3-D density structures is laborious. Much of the work described here takes advantage of the easiest contrasts to distinguish using automation: those between metal, silicates, and empty space (voids).

Volumes of individual CAIs and chondrules separated from their host meteorites were determined quantitatively using IDL routines. For each voxel row (e.g., constant y), in each x-y plane (constant z), the object was approached from both directions (e.g., minimum x and maximum x). A predetermined threshold for the density of air, allowing for noise in the signal, was used to remove all voxels external to the sample from consideration. That is, from all edges of the rectilinear analysis file volume, the code looked for the edge of the sample. Having found the sample edge, the code then determined the sample volume. Void spaces were measured by counting all voxels within the sample that had attenuation similar to air (Murray et al. 2003).

We have used several software products in developing tools for image analysis of tomographic stacks. Each tool has strengths and disadvantages. The large size of the data in any form makes a 64-bit operating system and application advantageous. Several actions are basic to working with images. To *threshold* pixels in a volume, we determine a pixel cut-off value *x* and produce a binary image setting all values above *x* to 1 and below *x* to 0. Thresholding of multiple pixel value ranges is an obvious extension. To *segment* an image or stack of images, rules are applied to combine contiguous pixels or voxels into blobs or other shapes. For example, segmentation would be used to fit a 3-D curve to the outer surface of an object in air. Filtering of images can be useful in reducing noise prior to image segmentation. A huge armamentarium of image analysis techniques lies ready for deployment in analysis of 3-D tomographic data.

Tiff stacks produced as discussed above can be imported into the 32- or 64-bit Imaris software package (Imaris 2007) and volumes segmented or rendered with remarkable visual effects. We have used Imaris to isolate metal grains in CR chondrules and to measure chondrule volumes and surface

areas (Hertz et al. 2003). On the DVD (DVD Fig. 3j) is an example of thresholding and segmentation of metal in a Renazzo chondrule (chondrule 1 of Hertz et al. 2003) produced in Imaris, from the tiff stack (DVD Fig. 3a, C1-tif).

The program Image/J is an open-source Java port by Scion Corporation, of NIH Image, the public domain software developed at the National Institutes of Health (ImageJ 2007). A large community of Image/J users has developed plug-ins and Pascal source code for a wide variety of image analysis tasks within the program. We have used Image/J to:

- define regions of interest or to cut out individual chondrules from image stacks frame by frame (Hertz et al. 2003);
- to filter, threshold, and measure volumes to obtain metal, void, and silicate proportions;
- to establish pixel cut-off values for processing volumes in IDL; and
- to determine best-fit ellipsoids to chondrule perimeters (Hylton et al. 2005).

We have used the IDL software (RSI 2007) to develop image analysis tools portable to 64-bit processors. This high-level language is optimized for array manipulation; many user-contributed routines are freely available. An advantage is the IDL Virtual Machine, in which precompiled codes can be run without a license. For example, the tomography group at the University of Texas, Austin, Texas, USA (Carlson et al. 2003) has developed a program called "blob3D" for segmenting objects such as vesicles, phenocrysts, or porphyroblasts from host rock (e.g., McCoy et al. 2002, 2003; Benedix et al. 2003). We have used blob3D to separate three components—metal/sulfide, chondrules and CAIs, and matrix—in Allende, and to quantify the chondrule(+CAI)-to-matrix ratio (Schoenbeck and Ebel 2003) (DVD Fig. 5d). This works in Allende because the FeO-rich matrix has high contrast relative to clasts. In ordinary chondrites, we have not been successful in writing a general algorithm that can automatically segment chondrules. Although the eye can easily discern chondrule boundaries in Semarkona (DVD Fig. 6) or Krymka (DVD Fig. 7), particularly in moving images, automation is a very challenging algorithmic problem.

Verification by Sectioning and Mapping

Following tomographic sectioning, samples (e.g., Allende, Fig. 3) (DVD Fig. 5) were cut on a precision wire saw (Princeton Instruments WS22). For serial sectioning, one side of each sample was polished. X-ray and BSE maps at 4 to 8 square μm/pixel were obtained using the 5-spectrometer Cameca SX100 electron microprobe at AMNH. The polished side was then epoxied to a 1-inch round glass slide cut along a chord so a supporting rectangular slide could be glued beneath it with a dissolving glue (DVD Fig. 15a). This assembly was glued to the head of a goniometer attachment on the saw, allowing good control of the wire path. Both the goniometer assembly and the wire move during cutting. We used either 20, 30, or 50 μm diameter tungsten wire carrying a slurry of submicron boron nitride in oil. Microscopic (~10 μm) flakes of the wire are left on a fresh surface and are removable by using a sonic cleaner prior to diamond lap polishing. With proper tensioning of the wire, a very smooth, flat cut is obtained, and the wire does not wander around refractory or metallic grains (e.g, in Renazzo). Samples such as the bulk meteorite pieces described here were cut through in 3–8 h using our tensioning scheme, with manual application of abrasive every 15–30 min.

APPLICATIONS

Distribution of Chondrules and CAIs in Allende

A 1.53 g slab measuring ~5 × 7 × 18 mm was cut from the oxidized CV3 carbonaceous chondrite Allende (AMNH 4948). Four tomographic image sets, stacked vertically 4.3 mm apart, each 720 angles by 650 × 309 pixels, were obtained at 42 keV X-ray energy and 17.094 μm/voxel edge spatial resolution. Each of the four sets was reconstructed separately to make density map volume files 255 MB in size. These were combined to make a whole volume (~1 GB), which was then cropped in IDL to 232 MB (Ebel 2007). Tiff image stacks were produced from the cropped volume file. These images are on the DVD (DVD Fig. 5a). Using a 30 μm wire, ten serial sections, each 50–150 μm thick, were cut parallel to an 18 × 7 mm face of the sample (face A of Fig. 3; DVD Fig. 15a). Sections were mounted with epoxy to 1-inch glass slides, polished, and mapped for the elements Al-Si-Fe-Ni-Ti-Mg-Na-Ca-S, and K or Mn, at 4–5 μm/pixel (selectively included on DVD as DVD Figs. 5b and 5c; see also Ebel 2007). This sample is described in detail below.

Several types of image results for this sample "Allende2" are contained on the DVD. Stacks of 8-bit tiff images are perpendicular to *x* and *z* axes. Combined X-ray maps (Mg = red, Ca = green, Al = blue) and BSE images of entire sections are from serial slices nearly parallel to tiff images X_*n* (DVD Figs. 5a and 5b) (Ebel 2007). In DVD Fig. 5b, a BSE map, X-ray map, and tomographic "slice" are compared. The X-ray map is a composite red-green-blue superposition of Mg, Ca, and Al intensities, respectively. The tomographic slice is the closest match to the BSE. Because the sample could not be physically cut and polished exactly parallel to the tomographic slice, there is not an exact correspondence between the EMP images and the tomographic image. Nevertheless, this image sequence illustrates the power of the technique to capture the essential texture, and by inference the mineralogy and chemistry, of the bulk sample.

Chondrules and CAIs are relatively easy to distinguish from matrix in these tomographic images due to the relatively high, uniform FeO content of Allende matrix. Because of this high contrast, it is possible to segment these images

automatically and to isolate chondrules from matrix at a high confidence level. Preliminary work (Schoenbeck and Ebel 2003; Ebel et al. 2004) demonstrates chondrule/matrix volumetric ratios of 0.17 and 0.38 in adjacent ~1 cm^2 volumes of Allende (DVD Fig. 5d). An mpeg movie (DVD Fig. 5g) illustrates a segmented volume file corresponding to the primary data (DVD Fig. 5e) through sample Allende2 perpendicular to the *x*-axis. Metal and sulfide can easily be distinguished from silicate. In the segmented view, chondrules are gray, metal and sulfide are white, and matrix is black. In detail, metal can be segmented from sulfide and/or magnetite because metal has much higher X-ray attenuation. We have not been able to discern iron sulfides from iron oxides (e.g., troilite from magnetite).

Distinguishing chondrules from CAIs is difficult in tomography because the higher X-ray attenuation of Ca-rich minerals can be identical to that of slightly ferrous magnesium silicates. However, type A CAIs and amoeboid olivine aggregates (AOAs) can be distinguished by their nonspherical shapes and their higher X-ray attenuation relative to Fe-poor chondrules (DVD Figs. 5a, 5e, and 5f). Type B CAIs may be distinguished by their large size and spherical shapes, but may be confused with large chondrules.

Chondrule Layering and Metal Distribution in CR Chondrules

There are a number of intriguing issues regarding the origin of components in the primitive CR chondrites that can best be addressed by 3-D petrologic techniques. CR chondrite metal grains have compositions suggesting that many have not been modified by parent body metamorphism and may therefore record primary nebular processes (e.g., condensation, melting, and/or reduction), thereby possibly providing clues to chondrule precursors and chondrule evolution. Some chondrules in CR chondrites are concentrically layered, indicating accretionary growth of individual chondrules. Chondrule shapes (convolution index) have been used to infer the degree of melting of the chondrules. To address these issues, it is essential to obtain precise data on physical properties such as chondrule shape, size, and structure, as well as distribution and abundance of metal. However, previous studies have been confined to the 2-D areas of polished thin sections, which provide apparent values and are in some cases misleading. Application of 3-D petrology can provide actual values for shapes and abundances and is clearly more appropriate for observing physical properties of chondritic components.

A roughly tetragonal prismatic fragment (~8 × 8 × 15 mm, 1.636 g) of the Renazzo (CR2) carbonaceous chondrite was chosen for tomographic analysis (AMNH 588). Two stacked volumes 4.0 mm apart were imaged at 17.11 μm/voxel edge in a 658 × 236 pixel field of view at 50 keV with a 3 s exposure time. Initial minimum and maximum attenuations of −3898, 20,817 were truncated to −500, 8000; the data set was rotated 45° to produce the images on DVD (DVD Figs. 8a–c). High X-ray attenuation is white in these images and represents metal grains surrounding and included inside chondrules. The distribution and volume fraction of this metal can be quantified (Hertz et al. 2003). An apparent compound chondrule pair (c4 + c5 in Fig. 6; DVD Fig. 3b) is shown in tomography frames in Fig. 7 and is discussed below. Multiple concentric layers of silicates and metal can be observed in some chondrules (see mpeg, DVD Figs. 8b–d).

Concentric layering in chondrules is particularly well-developed in the CR chondrite Al Rais (Weisberg et al. 1993) (Fig. 8). This texture has been interpreted as progressive accretionary growth of chondrules (Prinz et al. 1985). An entire 1.444 g specimen of Al Rais (AMNH 4168) was imaged at 17.11 μm/voxel edge in two stacked volumes 4.0 mm apart, for a combined volume file of 400 MB. From a volume cropped to 561 × 521 × 472 pixels (232 MB) with grayscale attenuation values from −6098 to 22,066, tiff stacks and movies were made in 8-bit grayscale ranging from 0 to 10,000 (DVD Fig. 1) (Ebel 2007).The sample was cut with a wire saw, with a smaller piece (Al Rais-B2) being imaged at 6.56 m/pxl in 3 stacks 3.0 mm apart for a total cropped volume of 426 × 426 × 1431 pixels (655 MB). At this higher resolution, chondrule layering is strikingly detailed and textural variations between chondrule core and rim layers can be accurately measured to help resolve the formation of the rim layers and their relationship to the chondrule core (DVD Figs. 1c and 1d) (Ebel 2007).

Compound Chondrules: Products of Nebula Collisions or Parent Body Compaction

The frequency and types of compound chondrule pairs have for good reason been promoted as useful indicators of the dynamic and thermal environment of chondrule formation (e.g., Desch and Connolly 2002). In tomographic images of this particular piece of Renazzo, we found a chondrule pair that appears compound (Fig. 6; DVD Fig. 3b). This pair is illustrated in orthogonal frame images in Fig. 7, where the whole volume (x = 1:412, y = 1:462, z = 1:472) has been cropped to (x = 210:325, y = 130:230, z = 250:360), so subframe x_60 corresponds to full frame x_271, and so on. At the resolution of tomography, it is not clear whether this pair has a septum of fine-grained matrix trapped between them. Wasson et al. (1995) established the criterion that trapped dust (matrix) between chondrules in a compound pair indicates that the pair formed on a parent body, not by collision between the two chondrules freely floating in space. Using tomographic images, we were able to cut this pair precisely to expose the dust septum between them (BSE image in Fig. 6; X-ray maps in DVD Figs. 8d–i). As can be seen in Fig. 7, there is a subset of possible random cuts through this piece of Renazzo that would make this compound pair appear to be a

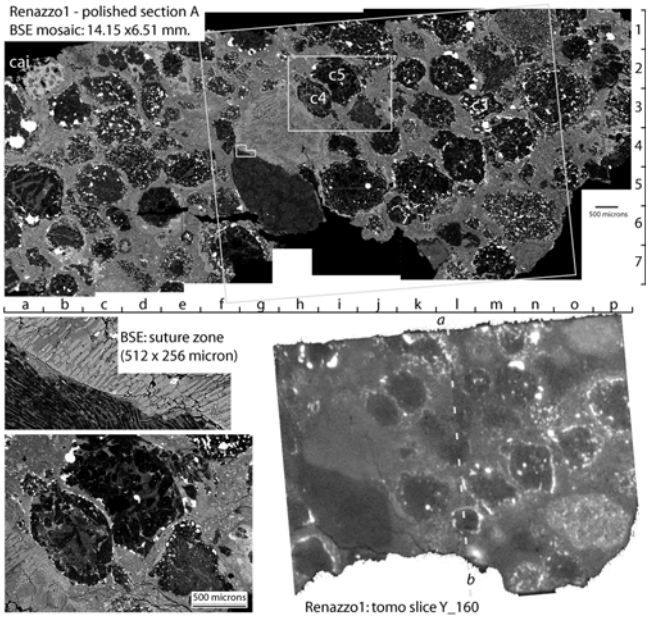

Fig 6. BSE image of cut Renazzo surface, with tomo.

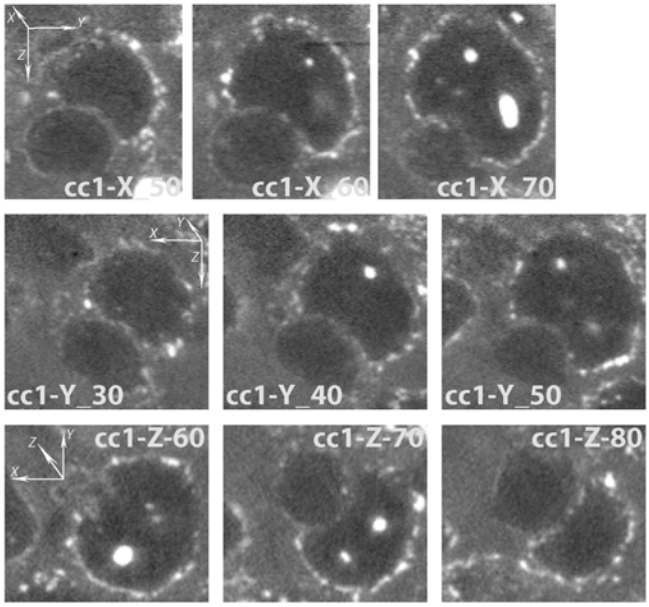

Fig 7. Orthogonal views of compound chondrule in Renazzo.

chondrule within a chondrule in certain thin section orientations. Ciesla et al. (2004) have shown the pitfalls of such interpretations. Here the outstanding question is: How did the one chondrule wrap so plastically around the other as the result of a parent body process?

By exploring tomographic and thick section images of Renazzo, chondrules were categorized according to their degree of contact and an extended classification scheme for compound chondrules was explored (Hylton et al. 2005). Compound chondrules are exceedingly difficult to find and characterize using 2-D petrographic (thin section) methods (Wasson et al. 1995; Ciesla et al. 2004). However, in the 3-D tomographic images, compound chondrules can be identified in CR chondrites due to the high contrast between metal on chondrule rims and adjacent matrix (Hertz et al. 2003; Hylton et al. 2005). Our preliminary results indicate that compound objects are more abundant than previously reported in CR chondrites. Additionally, we found that many chondrules in Renazzo are part of a network of "touching" objects, possibly the result of compaction on the CR parent body.

Our images of Allende also reveal compounds (DVD Fig. 5), but many compound chondrules must escape this level of analysis (Wasson et al. 1995). We have, for example, identified compounds in a thin section of NWA 487 that cannot be seen in tomographic data (DVD Fig. 10). Tomographic analysis at the highest possible resolution, followed by serial thick-sectioning, appears to be the best way to nondestructively locate compounds. This is an incredibly labor-intensive task, but the thick sections and data remain available for application of multiple techniques in the future.

The LL3 chondrite NWA 505 has been inferred to be rich in compound and aggregated chondrules, with >26% compound in 2-D thin section, uncorrected for 3-D effects (cf. Wasson et al. 1995), as distinct from, for example, Semarkona (Lauretta et al. 2002). We obtained tomographic images of the LL3 chondrite NWA 487 (AMNH 5021), which has a texture similar to NWA 505. Five stacked volumes 4.6 mm apart were imaged at 17.036 μm/voxel edge in a 650 × 285 pixel field of view at 45 keV. Images are included on DVD (DVD Fig. 10) (cf. Ebel 2007). In 3-D, chondrules that might appear "joined" in 2-D appear to be pressed together tightly and not truly "compound" in the sense of Wasson et al. (1995) and Gooding and Keil (1981). Boundaries between individual chondrules in this chondrite appear to approach the 120° angles typical of compacted terrestrial rocks and more highly processed chondrites (e.g., Itqiy; see below). We have not identified what particular measurement would quantify this qualitative observation, in contrast to the same measurement in, for example, the LL chondrite Semarkona (DVD Fig. 6). Comparing the two sets of images, it appears that NWA 487 samples a much more compacted parent body region than Semarkona. These two meteorites could be from different depths in the same parent body.

Crystal and Void Geometry and Possible Impact History of a Type B1 CAI

Voids (or vesicles) in rocks are significant in understanding the behavior of volatiles during crystallization, possible secondary chemical processes such as dissolution or vapor deposition, or mechanical processes such as internal fracturing due to shock events. Voids in chondrules and CAIs have been observed in chondrite thin sections. However, it is difficult to determine if these are natural voids that developed

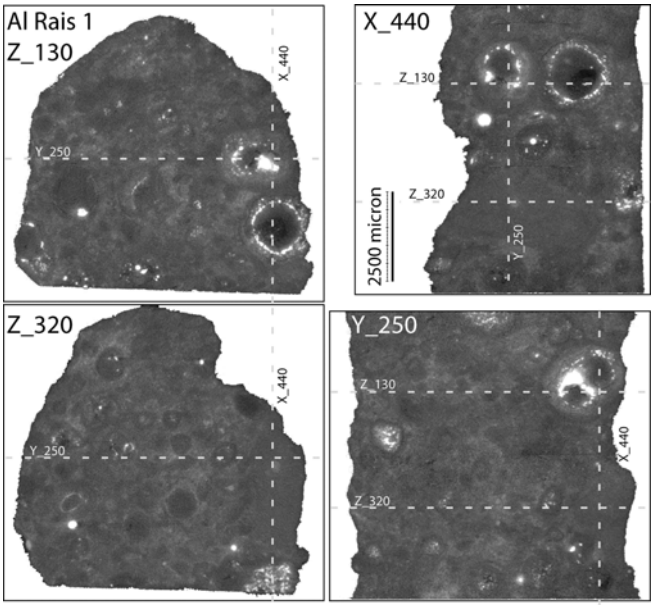

Fig 8. Orthogonal tomographic frames or "slices" through Al Rais.

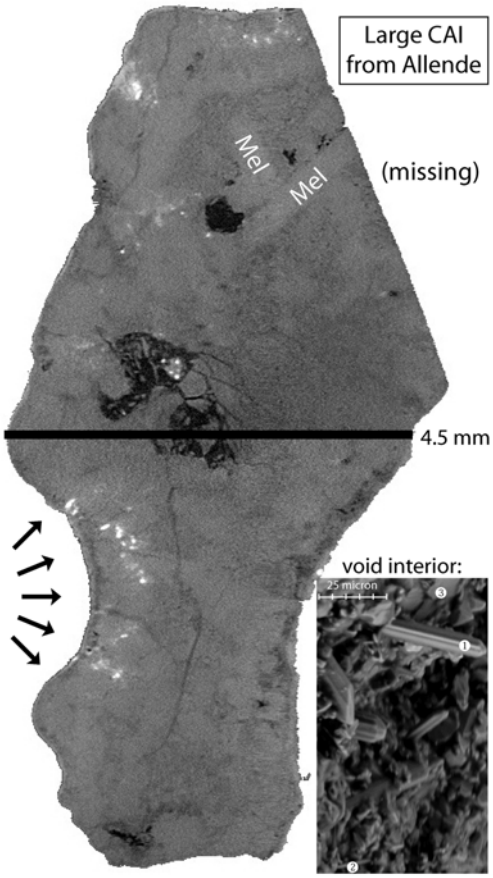

Fig 9. Allende CAI-1, with inset.

during chondrule or CAI formation or are the result of sample preparation. Tomographic 3-D imaging is advantageous for unequivocally determining natural voids in chondritic components.

A large type B1 CAI (AC1) was observed in a chip of Allende (AMNH 4308) and was separated from matrix with dental tools (Murray et al. 2003). The CAI is very irregular in shape (~4.5 mm in diameter by ~9 mm in length) and is missing a portion sawed from one end. The portion removed is inferred to be a small part of the CAI volume. Tomographic analysis of the whole uncut CAI was done at a spatial resolution of 10.24 μm/voxel edge, at 30 keV, in two data sets 4.0 mm apart (DVD Fig. 11). The CAI was then cut lengthwise into six slivers using a wire saw 30 μm thick; images at 4.4 μm/pixel were obtained on each sliver. These images have been combined into very large, high-resolution volumes of the object (Ebel 2007). Polished surfaces of these slivers have been X-ray mapped and analyzed. Subhedral tabular melilite crystals grow inward from the surface ("Mel"; Fig. 9), abundant anhedral fassaitic pyroxene is interstitial to melilite and rarely touches the CAI surface, 2–15 μm spinels are superabundant, and one large anorthite grain was found. The spinels are not distinguishable in the tomographic images (DVD Fig. 11), and only the very largest ones are clearly visible in tomographic images of cut slivers at a resolution of 4.4 μm/pixel. Trails of disseminated sulfide are observed with some local concentrations. Tomography is an ideal method to search for PGE-rich fremdlinge (El Goresy et al. 1979) due to their predicted very high X-ray attenuation (Fig. 5c). So far, we have not been able to pick out any fremdlinge in our images, and energy dispersive spectrometric (EDS) analyses have not revealed PGE in exposed surfaces of any of the CAIs we have studied. Fine-grained rims sequences (Wark and Lovering 1977) are generally too thin to discern sequence thicknesses in tomographic images of CAIs.

In the tomographic images, as in the BSE images of actual cut surfaces, the distinction between fassaite and melilite is clearly visible (Fig. 9). This is due to the higher X-ray attenuation of Ca in the melilite relative to fassaite (Fig. 5a). Tomography, verified by surface analysis, reveals how tabular melilite crystals extend from the CAI rim inward, with fassaite occupying anhedral internal space in this type B1 CAI (Grossman 1975; Richter et al. 2002). Thresholding and segmentation of these minerals was attempted. The resulting binary images (DVD Fig. 11c) clearly illustrate melilite crystallization from the rim inward; however, the distinction between minerals does not permit a quantitative analysis of their relative proportions.

One very obvious feature of this CAI is the abundant void space, which is black in the tomographic images (DVD Figs. 11a and 11b). Voids extend very irregularly throughout the sample and are measured to be approximately 3.0% of its $V^{tot} = 83.6\ mm^3$. Voids contain brecciated material, primarily fassaite, which is evident on cut samples. Voids appear to occur preferentially between the melilite tablets, and in no case appear to crosscut melilite. Voids are observed to connect to the CAI surface only through very thin, snaking channels

almost below our spatial resolution of 10.24 μm/voxel edge. BSE and EDS analyses of void walls revealed euhedral crystals (Fig. 9, inset) similar to those in Allende type A CAI CG-11 (Allen et al. 1978): 1) elongate nepheline ($NaAlSiO_4$), some striated, 10 μm thick to 35 μm long; 2) wollastonite ($CaSiO_3$) whiskers to 15 μm long; and 3) platy grossular ranging from 10–15 μm. Wollastonite is abundant, intergrown with euhedral grossular ($Ca_3Al_2Si_3O_{12}$) crystals. All of these are refractory products of high-temperature reactions adding Na and Si oxides to the primary Ca-aluminosilicate CAI mineralogy.

Less obvious but still compelling is the evidence that this CAI experienced one or more impacts. Such an interpretation could only result from 3-D tomographic evidence (DVD Fig. 11). Examining the lower left part of the CAI through slices perpendicular to a *y*-axis, there is a clear semicircular depression in the CAI. In the CAI, metal sulfide is superabundant along what appear to be injection fractures in the CAI emanating from the inferred impact site. A similar concavity is evident on the right side of the CAI but lacks this injection feature. A highly speculative interpretation would be that the CAI was partially molten when it was impacted on both the left and right sides, causing not only the impact depressions, but also a volumetric disturbance resulting in the brecciated void space that is visible in the half of the CAI that is above the impact depressions. The nostrum that "textures lie" is more true for 2-D than for 3-D textural information. The ability to make such interpretations for CAIs and chondrules is dependent on 3-D information. Real processes occur in three spatial dimensions, so textural evidence of real processes should be sought from 3-D data.

Textural Features of Individual and Compound Chondrules

We separated numerous chondrules from matrix in order to image them at the highest possible spatial resolution. Tomographic data are presented as mpegs, made from density structures of chondrules from Bjürbole (L/LL4), Karoonda (CK4), Kakangari (K3), Renazzo (CR2), and Allende, at resolutions from 5 to 2 μm/voxel edge (DVD Fig. 3). Complementary data include tiff stacks through these objects and analyses of cut surfaces (Ebel 2007). To pass through a chondrule in 3-D is quite striking even to those who have examined numerous thin sections in the laboratory. Here we present a few highlights of our observations.

Fifteen chondrules separated from Karoonda were mounted individually and analyzed by tomography. A typical porphyritic olivine chondrule is Kr30. Tomographic data allows creation of an X-ray image, as if one were viewing the chondrule rotating in an X-ray beam (DVD Fig. 3e). Details visible in this X-ray image do not seem obvious in a finished image stack or mpeg, perpendicular to a particular axis (DVD Fig. 3f). An interesting curiosity of the X-ray image is that particular olivine crystals in this porphyritic olivine (PO) chondrule appear to "flash" at particular rotation angles. This occurs because there is an orientation at which an individual crystal is at the Bragg angle where it must constructively diffract the monochromatic X-ray beam.

Image stacks of Renazzo (DVD Fig. 8) were manually cropped to isolate chondrules of interest in rectilinear subvolumes (DVD Figs. 3a and 3j). A drawing tool in ImageJ was then used to isolate each chondrule in every slice in which it appeared. This resulted in a separate image stack for each of 8 chondrules. Metal abundances, shape parameters, and other parameters were subsequently measured by thresholding and segmentation of each chondrule image stack (Hertz et al. 2003) (DVD Fig. 3j).

A very large chondrule (BB1) was observed in Allende (AMNH 4294) and separated from matrix with dental tools. This revealed a second chondrule (BB2), which was also removed (Fig. 10a). Between the two was a thin septum of compressed matrix-like material, which was recovered intact. Although precluded by the criterion of Wasson et al. (1995), these chondrules constitute an apparently compound pair with a dust-rich septum. Each whole uncut chondrule and the septum were attached to plastic rods; tomographic images (DVD Fig. 3c) were collected at spatial resolutions of 12.92 (BB1, at 35 keV) or 9.55 μm/voxel edge (BB2 and septum, 40 keV). Each chondrule was then cut with a diamond saw; polished thick sections were analyzed on the electron microprobe and field emission scanning electron microscope (SEM) at the AMNH.

The chondrule pair consists of a relatively smooth, near-perfectly spherical radiating pyroxene (RP) chondrule 8 mm in diameter (BB1) and a layered porphyritic pyroxene-olivine chondrule 5 mm in diameter (BB2). BB1 has no metal or sulfide, and a single concave depression 3 mm in diameter and 0.5 mm deep (Fig. 1a) occupied by the slightly smaller ovoid BB2. BB2 has pyroxene and olivine phenocrysts (average Fa12, Fs7) with abundant sulfide associated with Fe-rich silicates (to maximum Fa18, Fs21). BB1 and BB2 are separated by a septum (~0.6 mm) of rim-like material, suggestive of dust trapped between them either in space or after their slight separation and dust infilling on the Allende parent body. The criterion of Wasson et al. (1995) of "no matrix between" true compound chondrules requires extraordinary parent body processes in both cases (Renazzo c4-c5, Figs. 6 and 7; Allende BB1-2, Fig. 10) illustrated here. Tomographic imaging of compound objects reveals features that warrant further work, particularly a comparison of the dust between compound objects compared with outlying matrix dust.

The modes of occurrences of void spaces are very different in each of the compound chondrule pair. In BB1, voids are thin (30 μm), elongated (1–3 mm) lenses parallel to the radiating pattern of the pyroxene (Figs. 10b and 10c). After thresholding the image, voids are measured to be 0.05%

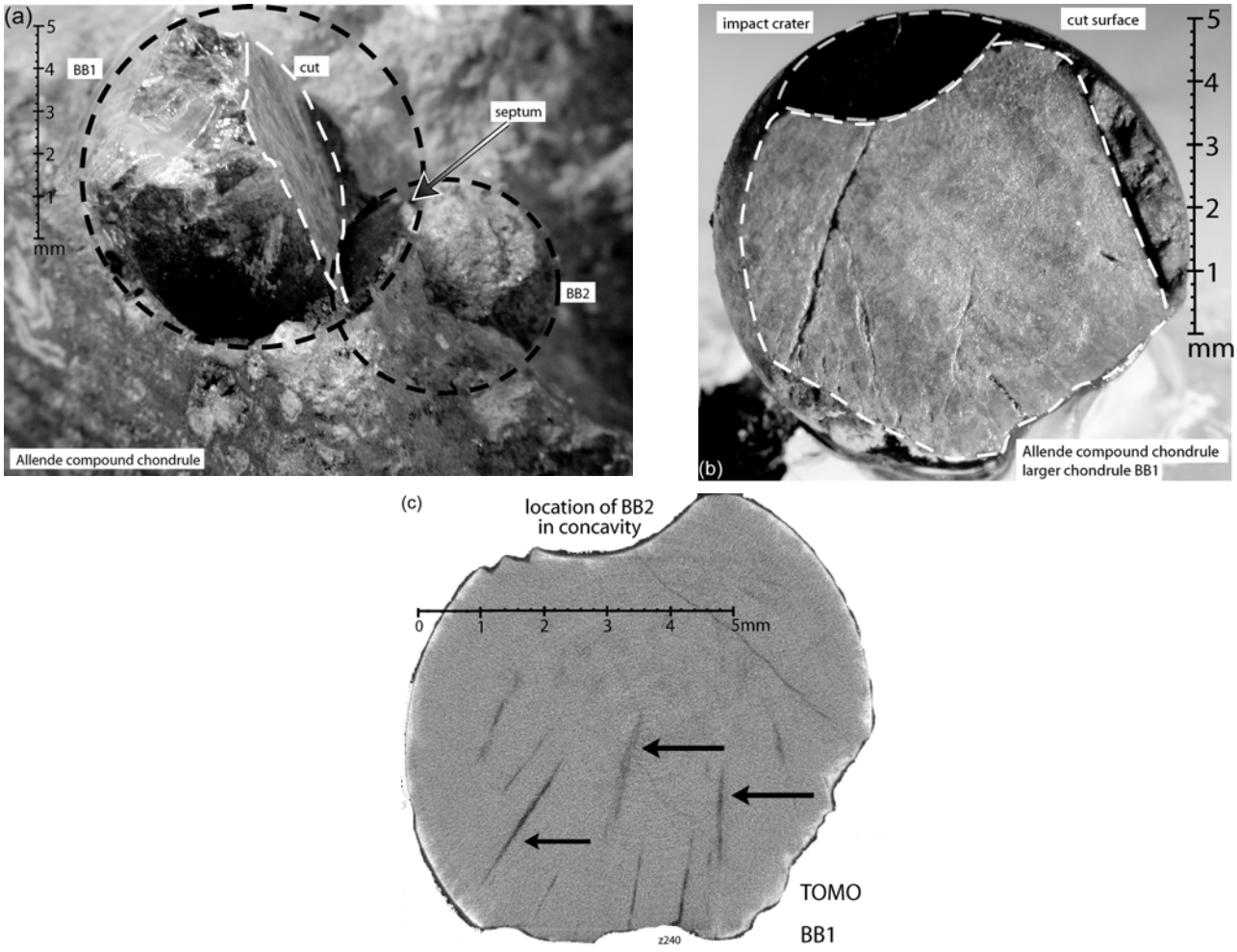

Fig 10. a–c) Compound chondrule pair from Allende.

of the total volume of BB1 (V^{tot} = 204.1 mm^3). Similar void textures were reported in an Efremovka RP chondrule by Krot et al. (2002, their Fig. 9f), where voids also appear thin and elongate between the pyroxene crystals. In BB1, the voids and crystal orientations suggest that the entire chondrule crystallized from a supercooled droplet in a very short time. Successive tomographic images indicate, by alignment of these voids, that pyroxenes radiate from a point very close to or on the rim of the circular concavity with the same radius of curvature as BB2. This suggests that the impact in space of solid BB2 with supercooled BB1 initiated crystallization of the latter.

In BB2, voids occur in two ways. One type (#1, Fig. 10e) occurs as small, roughly spherical voids near the boundary between inner, coarse FeO-poor silicates and the outer FeO-rich zone. The second is a large, very irregular void in the central zone (#2, Fig. 10e). All voids account for 0.61% of BB2's V^{tot} = 58.6 mm^3. In a plagioclase-olivine inclusion from Maralinga (CK), Kurat et al. (2002, their Figs. 3–5) reported on similar pore spaces in plagioclase, filled with olivine and feathery carbonates. It is not clear whether these voids in BB2 formed in space or on a parent body. This compound pair illustrates the union of an "old," solid PO chondrule with a "young," hot, plastic, supercooled chondrule that instantly crystallized to an RP chondrule.

Location of True Crystal Cores and Rims, and Modal Analyses

The basaltic shergottite Zagami is dominated by strongly zoned, oriented pyroxene laths. The petrologic evidence has been interpreted differently by different investigators, as summarized by McCoy et al. (1992; cf. Stolper and McSween 1979). McCoy et al. (1992) described two Zagami lithologies and concluded that pyroxene cores formed at depths >7.5 km and rims at shallower depths. Lentz and McSween (2000) studied pyroxene crystal size distributions (CSD) and textures in thin section. Of the six shergottites they studied, Zagami and Shergotty had the most complex CSD curves with kinks suggesting multiple stages of crystallization, which is in agreement with the scenario of McCoy et al. (1992). Wadhwa (2001) determined Eu and Gd abundances in pyroxene cores

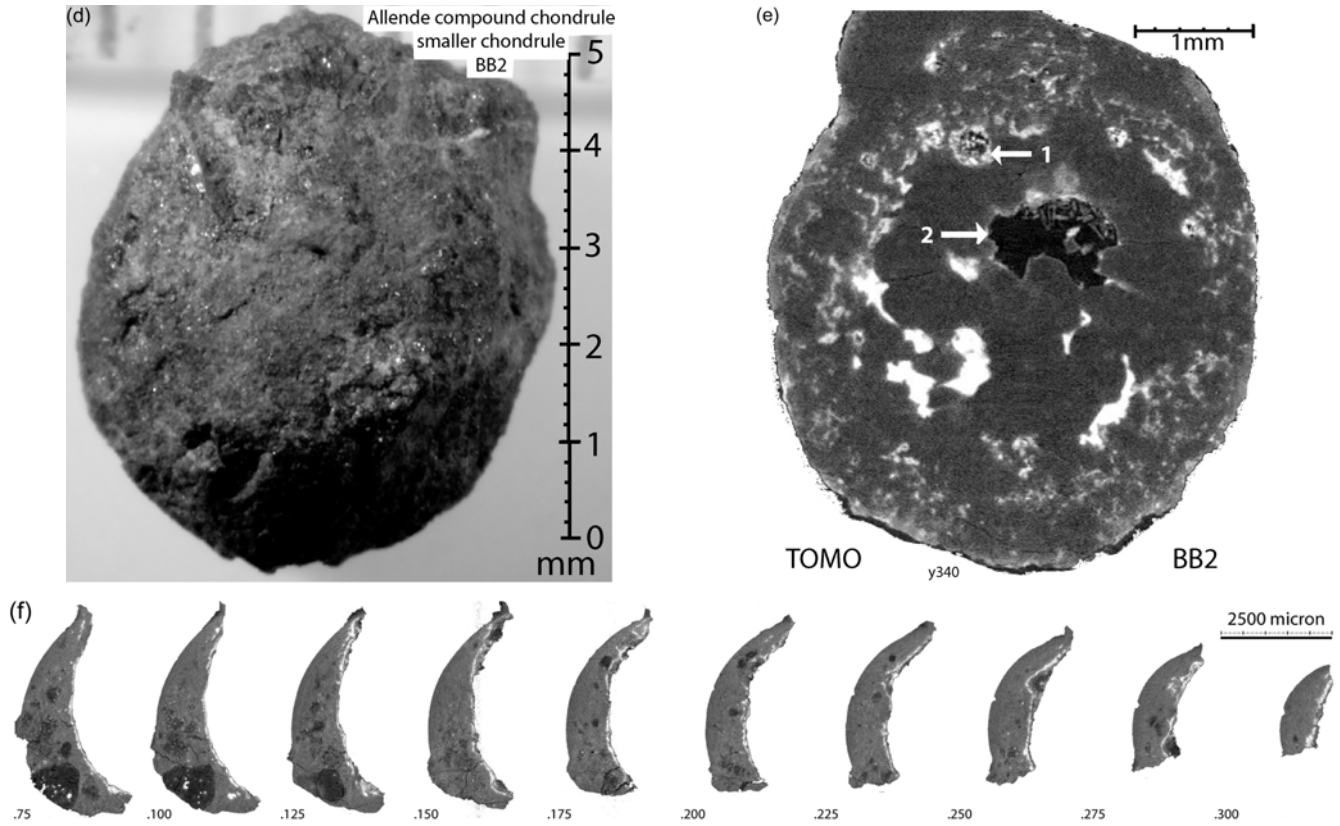

Fig 10. *Continued.* d–f) Compound chondrule pair from Allende.

(inferred from 2-D chemical mapping) and used this evidence to calculate the oxygen fugacity of the Martian mantle.

To explore how tomographic imaging can verify and supplement studies of this kind, a 0.255 g rectilinear piece measuring ~5 × 7 × 18 mm was cut from Zagami (AMNH 4709). Two vertically stacked tomographic image sets, 720 angles by 650 × 488 pixels, 4.8 mm apart, were obtained at 42 keV and 10.50 μm/voxel edge spatial resolution. Reconstructed volumes were combined to make a whole volume, which was then cropped to 232 MB (Ebel 2007). Image stacks were produced from the cropped volume file by thresholding to a range of –500 to 8000 (ts1) from the original grayscale range of –4824 to 9707. Movies from these images are on DVD (DVD Fig. 4) (cf. Ebel 2007 for tiff stacks). Using a tungsten wire 30 μm in diameter, a thick section was cut and polished parallel to a 5 × 10 mm face of the sample and mapped in BSE on the AMNH FE-SEM.

Pyroxene morphology and chemical zoning in Zagami are visible in tomographic images. Homogeneous magnesian cores are darker (less attenuating) than FeO-enriched, zoned rims (cf. McCoy et al. 1992, their Fig. 3). Grain size and orientation can be determined to a high degree of accuracy from the tomographic images. Also visible in the tomographic data are the 3-D sizes, abundance, distribution, and associations of oxide grains. Analyses such as those by Wadhwa (2001) depend strongly on the location of mineral grain cores in polished section and knowledge of the depth to the buried rim. Rims and cores of pyroxenes are readily distinguished by eye in the 3-D tomographic images of Zagami, especially in moving through image stacks. For a particular cut through the sample, grain geometry can be verified by surface analysis. The depth of the core regions of individual crystals (in microns) can then be determined from tomographic images orthogonal to the cut surface. This complementary technique would allow for more accurate interpretation of data obtained using ion probe or laser ablation methods, that excavate holes up to 100 μm deep in individual grains. Selection of crystal rims can also be optimized in 3-D using tomography.

McCoy et al. (1992) determined areas of pyroxene cores by analysis of BSE image mosaics. Although rims and cores can be distinguished by eye in tomographic images, attempts to quantify the relative volumes of core and rim pyroxene using automated counting of tomographic volumes were not successful due to dark noise in the lighter rims and light noise in the darker cores. A thresholding exercise on a stack of 8-bit images (normal to *x*) yielded proportions of maskelynite, pyroxene (plus mesostasis), and opaques (oxides and sulfides). Bright (high attenuation) opaque phases were easily separated and found to be 2.9% of the volume, compared to 2.1 by Stolper and McSween (1992) and an average of 2.5 for four UNM samples (McCoy et al. 1992). After subtracting air,

it remains to threshold maskelynite (darker, lower attenuation; diamonds, Fig. 11) from pyroxene and included mesostasis (solid squares, Fig. 11). Figure 11 shows how modal separation of these phases depends on the grayscale chosen for thresholding compared to values reported previously. By visual inspection, a grayscale of 81 was chosen before reference was made to the earlier work. This measurement is thus most consistent with that by Stolper and McSween (1979) (solid stars in Fig. 11), but not far from that reported for the sample UNM 992 of McCoy et al. (1992) (open stars in Fig. 11).

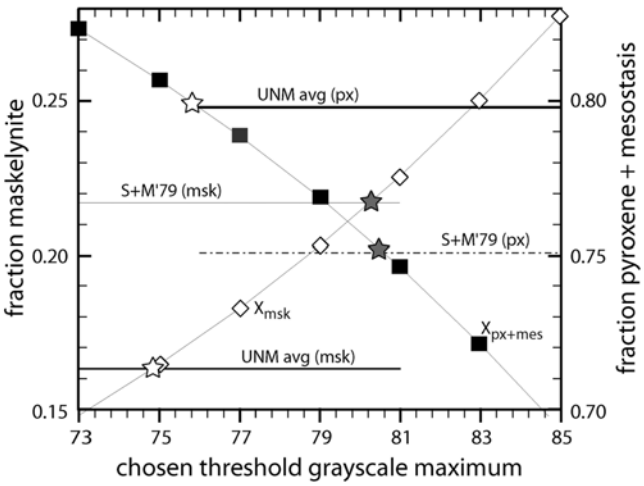

Fig 11. Modal analysis of Zagami.

Location of Potential Inclusion-Bearing Phenocrysts in Lunar Spherules

We have extended our work on meteorites to other extraterrestrial samples, such as location of dust in aerogel (Ebel and Rivers 2005) (DVD Fig. 13). Another application is in finding phenocryst-bearing spherules in samples of lunar soil that consist of glassy spherules from fire-fountain eruptions (Ebel et al. 2005). Weitz et al. (1999) reported a single ~450 μm, equant olivine phenocryst containing four glassy melt inclusions (or inclusion cores), the largest of which being ~30 μm in size, in a thin section of the Apollo 17 74001/2 drill core. The melt is thought to sample the parent magma of the lunar basalts at a depth of ~400 km, as deduced by the S content of the inclusion (600 ppm), which is 400 ppm greater than that of the orange glass host (Weitz et al. 1999). Melt inclusions potentially contain a full complement of the volatile components of the parent magma, which can be analyzed by infrared and raman spectroscopy. Although the A17 orange glass magma is thought to derive from a depth of ~400 km (Green et al. 1975), other calculations imply a depth of 4 km of graphite oxidation (and melt saturation in C-O volatiles) during ascent (Weitz et al. 1997).

Approximately 200 loose spherules were placed in a crease of cellophane paper and picked up on 4 0.2 × 1 × 60 mm plastic strips coated with ambroid (a modeling glue that dissolves completely in ethyl acetate). Strips were imaged using 15 keV X-rays at a spatial resolution of 1.96 μm/voxel edge (DVD Fig. 14) (cf. Ebel 2007). Surface effects (e.g., along the plastic substrate) appear as bright lines at this spatial resolution due to reflection when incident X-rays are at very small angles to these surfaces. Some internal features of spherules are not phenocrysts, but instead are fine microcrystals formed when the spherules were quenched from liquid to glass.

Visual inspection of tiff image stacks and stacks made into mpegs revealed at least one phenocryst in a single spherule in segment C of sample OG1. The olivine is dark (lower attenuation) relative to brighter, Ca-, Fe-bearing glass and has a euhedral outline. This spherule was easily located under a microscope and removed from the aggregate, and X-ray diffraction of the whole revealed the phenocryst to be olivine. From tomography, there is no evidence of any glass inclusion in this olivine phenocryst, and this is the only unambiguous phenocryst we found. Other spherules contain metal grains. We also observed clasts that are not spherical and contain components with high (e.g., metal) and low (e.g., voids) attenuation. Some of the dendritic and barred textures seen in images of the spherules may be quench textures; these may allow constraints to be placed on the cooling histories of these spherules. A larger sample of spherules might contain phenocrysts with melt inclusions, allowing a determination of a few more data points relevant to the volatile composition of the ancient magmas of the moon.

CONCLUSIONS

The primary conclusion from this work is that 3-D sample analysis, even at low resolution, is the preferred first step in approaching all rare extraterrestrial samples (Flynn et al. 2000; Tsuchiyama et al. 2002). Tomography should inform the selection of where rare or unique specimens are sliced for surface (2-D) chemical analysis. This nondestructive analysis technique yields not simply a set of images, but information that the human brain can comprehend in a fundamentally different way as compared to standard, static, thin-section data. This kind of view is advantageous in comprehending the ways meteorites are put together and the subtleties of chondrule-CAI-matrix relationships. Many quantitative results can be generated from tomographic data; this prospect will no doubt improve in the near future.

A critical scientific interface is that between meteoriticists and astrophysicists (e.g., Desch and Connolly 2003; Cuzzi et al. 2001; Joung et al. 2004; Cuzzi and Alexander 2006). Textures recorded in meteorites are inherently 3-D material evidence for the dynamical regimes in which chondrules formed and meteorites were accreted. Tomography, in tandem with serial sectioning, promises an

abundance of such evidence in a form fundamentally richer than that provided by 2-D thin section studies alone. Size, shape, and compound chondrule statistical studies cry out for 3-D data sets. Tomography can add textural evidence useful in distinguishing nebular from parent body processes in CAIs and chondrules. Tomography addresses the intersection of chemical and physical studies of meteorite genesis.

Tomography is useful in analyzing individual chondrules and CAIs, but its greatest utility is in locating objects of interest and in the study of aggregates. The processes of asteroid lithification and the bulk movement of metal during the transition from low petrologic grade to high (e.g., L3 to L5) are poorly understood. These processes can be addressed using tomographic data. The aggregate of chondrite images (data) we have collected suggest that the chondrite record samples a continuum of differentially compacted materials. Perhaps some of this data will inform the beginning of an answer as to how asteroids become lithified and how asteroid textures might vary with depth.

Tomography offers the opportunity to obtain volume, size, and type statistics on chondrules with a new level of certainty. For example, volume percentages of components are important parameters in the descriptions of the various chondrite groups (e.g., Grossman 1988; McSween 1977; King and King 1978; Gooding and Keil 1981; Kornacki and Wood 1983). A limitation is that tomography does not offer a unique solution to the chemical identity of chondritic components where shape is not a determinant. Great efforts have been made in extending 2-D analysis of thin sections to valid 3-D quantification (Woronow and King 1985; Eisenhour 1996). In their classic work, Gooding and Keil (1981) laboriously applied serial sectioning approaches to this problem. Other workers (e.g., Genge and Grady 1998) have applied more traditional methods. Sampling bias is clearly a complicating factor, as seen in comparisons of analyses of disaggregated samples and of thin sections (e.g., Grossman et al. 1985; Grossman and Wasson 1982; Gooding et al. 1980). The DVD data sets appended to this paper (cf. Ebel 2007), provide observational results with which these issues can be addressed. Relative chondrule size is addressed in several prominent studies (e.g., Rubin and Keil 1984; King and King 1978, 1979; Rubin and Grossman 1987; Benoit et al. 1999; May et al. 1999). As with volume statistics, size determinations are problematic in thin section (Eisenhour 1996). Crystal size distribution techniques have recently become popular (Zieg and Lofgren 2003). All these would benefit from comparison of 3-D data sets with 2-D studies.

Chondrule shapes can be used to infer their thermal histories or to reveal their impact histories prior to parent body accretion. King and King (1978) studied chondrule circularity in polished sections. Hutchison et al. (1979) and Hutchison and Bevan (1983) found that elongated chondrules in Tieschitz were plastic or partially molten in situ in their parent body. Martin et al. (1975) found preferred orientations in four C3 chondrites. The preferred orientation of chondrules can be addressed in 3-D using tomography. Tomography of Renazzo (CR2; DVD Fig. 8) and Leoville (CV3r; DVD Fig. 12) illustrates the petrofabrics developed in these chondrites on their parent bodies. These effects can also be observed in thin section and in meteorite slices, but are ambiguous in 2-D. In all the meteorites we have studied using tomography, gross petrofabrics of this kind, if present, are observable in the tomographic data. In principle, tomographic data allows directions of stress to be ascertained in a particular sample by mapping of the axes of ellipsoids fit to the 3-D chondrule volumes.

Chondrule dynamics during crystallization were inferred by Tsuchiyama et al. (2000) from void and olivine plate distributions in individual oblate porphyritic and barred olivine chondrules. They concluded that these objects were spinning (~100 rpm) while partially molten. By 3-D imaging a suite of chondrules in situ, such information could be combined with orientation of obliquity to differentiate between nebular or asteroidal processes. That is, oblateness of individual chondrules due to spinning should be a random component of aggregate oblateness in the parent body and the meteorite. Oblateness due to parent body forces should have a strongly preferred direction, such as that observed in Renazzo and Leoville. Metal grains would be expected to accumulate around the equators of molten, spinning chondrules. We found no evidence in any chondrules in any CR chondrites studied for higher metal abundance on preferred equatorial planes.

A future goal of this work is to determine bulk compositions of chondrules and CAIs by coupling tomographic analysis with quantitative analysis of thin serial sections through tomography volumes. Our preliminary work shows that a much better approach to reality can be achieved using data from several serial sections, compared to data from a single section (Hertz et al. 2003; Ebel, in preparation). Furthermore, tomographic data can indicate the likelihood of success in such an enterprise by yielding the overall shape and distribution of macrocrystals (>40 μm) and also the overall shape and volume of the CAI. However, it is not likely that we will soon solve the problem posed by the heterogeneous distribution of 2–15 μm spinels in CAIs (Simon et al. 2002).

Sorby (1877) read the textures of chondrites in two dimensional thin sections and concluded that chondrules are “like drops of fiery rain” (i.e., multiple chondrule-forming events). Three-dimensional visualization by microtomography illustrates the textures of chondrites and their components in a way unappreciable by, and complementary to, thin section analysis. Metal migration, size distributions, and associations between objects become apparent. Quantification of these phenomena is difficult; we are only beginning to develop the tools. But, as did Sorby’s in two dimensions, our eyes and intuition will find pattern in the three-dimensional textures of the chondrites.

Acknowledgments–This manuscript benefited from helpful reviews by D. Heymann, J. Wood, and A. Tsuchiyama. We thank Joe Boesenberg and Michael Weisberg for technical assistance and discussion. The Itqiy sample was provided by W. Boynton of the University of Arizona. Thanks to Nehru E. Cherukupalli of Brooklyn College, who separated Karoonda and Kakangari chondrules from matrix, and Alex Bergin for separation and XRD of lunar spherules. Thorbjoern Schoenbeck (University of Cologne) serially sliced and mapped Allende and performed image analyses while on an Annette Kade Fellowship at AMNH. Students Sara (Baughman) Colvard and Shavonne Hylton were supported in analysis of Renazzo by a Research Experience for Undergraduates site grant from the U.S. National Science Foundation (AST 0243837) to the Division of Physical Sciences, AMNH. This research has made use of NASA's Astrophysics Data System Bibliographic Services. Use of the APS was supported by the U.S. Department of Energy, Office of Science, Office of Basic Energy Sciences, under contracts no. W-31-109-ENG-38 and DE-AC02-06CH11357. Research was supported by the American Museum of Natural History, and National Aeronautics and Space Administration grants NAG5-12855 and NNG06GE42G (D. S. E.).

Editorial Handling—Dr. A. J. Timothy Jull

REFERENCES

Allen J. M., Grossman L., Davis A. M., and Hutcheon I. D. 1978. Mineralogy, textures, and mode of formation of a hibonite-bearing Allende inclusion. Proceedings, 9th Lunar and Planetary Science Conference. pp. 1209–1233.

Arnold J. R., Testa J. P., Friedman P. J., and Kambic G. X. 1983. Computed tomographic analysis of meteorite inclusions. *Science* 219:383–384.

Attwood D. 2006. Nanotomography comes of age. *Nature* 442:642–643.

Benedix G. K., Ketcham R. A., McCoy T. J., and Wilson L. 2003. Vesiculation in ordinary chondrites due to impact melting: The "PAT" 91501 answers (abstract #1947). 34th Lunar and Planetary Science Conference. CD-ROM.

Benoit P. H., Symes S. J. K., and Sears D. W. G. 1999. Chondrule size distributions: What does it mean? (abstract #1053). 30th Lunar and Planetary Science Conference. CD-ROM.

Carlson W. D. and Denison C. 1992. Mechanisms of porphyroblast crystallization: Results from high-resolution computed X-ray tomography. *Science* 257:1236–1239.

Carlson W. D. and McCoy T. J. 1998. High-resolution X-ray computed tomography of lodranite GRA 95209 (abstract #1541). 29th Lunar and Planetary Science Conference. CD-ROM.

Carlson W. D., Row T., Ketcham R. A., and Colbert M. W. 2003. Applications of high-resolution X-ray computed tomography in petrology, meteoritics, and palaeontology. In *Applications of X-ray computed tomography in the geosciences*, edited by Mees R., Swennen R., van Geet M., and Jacobs P. Geological Society Special Publication #215. London: The Geological Society of London. pp. 7–22.

Carpenter P. K. and Gillies D. C. 2005. Analysis of iron meteorites using computed tomography and electron-probe microanalysis. *Microscopy and Microanalysis* 11:1344–1345.

Ciesla F. J., Lauretta D. S., and Hood L. L. 2004. The frequency of compound chondrules and implications for chondrule formation. *Meteoritics & Planetary Science* 39:531–544.

Cuzzi J. N., Hogan R. C., Paque J. M., and Dobrovolskis A. R. 2001. Size-selective concentration of chondrules and other small particles in protoplanetary nebula turbulence. *The Astrophysical Journal* 546:496–508.

Cuzzi J. N. and Alexander C. M. O'D. 2006. Chondrule formation in particle-rich nebular regions at least hundreds of kilometres across. *Nature* 441:483–485.

Desch S. J. and Connolly H. C., Jr. 2002. A model of the thermal processing of particles in solar nebula shocks: Application to the cooling rates of chondrules. *Meteoritics & Planetary Science* 37: 183–207.

Ebel D. S. 2007. Meteorites: Sample images and data. http://research.amnh.org/users/debel/meteorites and http://research.amnh.org/users/debel/tomo-aps/aerogel1.html. Accessed 15 April 2007.

Ebel D. S. and Rivers M. L. 2005. High-resolution 3-D local tomography of particle tracks and fragmentation in aerogel (abstract #5299). *Meteoritics & Planetary Science* 40:A42.

Ebel D. S., Schoenbeck T. W., and Palme H. 2004. 3-D tomographic measurements on Allende volumes—Constraints on the formation and accretion of chondrules and matrix (abstract #5153). *Meteoritics & Planetary Science* 39:A33.

Ebel D. S., Fogel R. A., and Rivers M. L. 2005. Tomographic location of potential melt-bearing phenocrysts in lunar glass spherules (abstract #1505). 36th Lunar and Planetary Science Conference. CD-ROM.

Eisenhour D. D. 1996. Determining chondrule size distributions from thin-section measurements. *Meteoritics & Planetary Science* 31: 243–248.

El Goresy A., Nagel K., and Ramdohr P. 1978. Fremdlinge and their noble relatives. Proceedings, 9th Lunar and Planetary Science Conference. pp. 1279–1303.

El Goresy A., Nagel K., and Ramdohr P. 1979. Spinel framboids and fremdlinge in Allende inclusions: Possible sequential markers in the early history of the solar system. Proceedings, 10th Lunar and Planetary Science Conference. pp. 833–850.

Feng H., Jones K. W., Stewart B., Herzog G. F., Schnabel C., and Brownlee D. E. 1999. Internal structure of two type I deep-sea spherules by X-ray computed microtomography (abstract #1209). 30th Lunar and Planetary Science Conference. CD-ROM.

Flannery B. P, Deckman H. W., Roberge W. G., and D'Amico K. L. 1987. Three-dimensional X-ray microtomography. *Science* 237: 1439–1444.

Flynn G. J., Rivers M. L., Sutton S. R., Eng P., and Klöck W. 2000. X-ray computed microtomography (CMT): A non-invasive screening tool for characterization of returned rock cores from Mars and other solar system bodies (abstract #1893). 31st Lunar and Planetary Science Conference. CD-ROM.

Flynn G. J., Keller L. P., Wirick S., Jacobsen C., and Sutton S. R. 2003. Analysis of interplanetary dust particles by soft and hard X-ray microscopy. *Journal de Physique IV* 104:367–372.

Genge M. J. and Grady M. 1998. The textures and abundances of chondrules in the Kakangari chondrite (abstract #1670). 29th Lunar and Planetary Science Conference. CD-ROM.

Gooding J. L. and Keil K. 1981. Relative abundances of chondrule primary textural types in ordinary chondrites and their bearing on conditions of chondrule formation. *Meteoritics* 16:17–42.

Gooding J. L., Keil K., Fukuoka T., and Schmitt R. A. 1980. Elemental abundances in chondrules from unequilibrated chondrites: Evidence for chondrule origin by melting of pre-

existing materials. *Earth and Planetary Science Letters* 50:171–180.

Green D. H., Ringwood A. E., Hibberson W. O., and Ware N. G. 1975. Experimental petrology of Apollo 17 mare basalts. Proceedings, 6th Lunar Science Conference. pp. 871–893.

Grossman J. N. 1988. Formation of chondrules. In *Meteorites and the early solar system*, edited by Kerridge J. F. and Matthews M. S. Tucson, Arizona: University of Arizona Press. pp. 680–696.

Grossman J. N. and Wasson J. T. 1985. The origin and history of the metal and sulfide components of chondrules. *Geochimica et Cosmochimica Acta* 49:925–939.

Grossman J. N., Rubin A. E., Rambaldi E. R., Rajan R. S., and Wasson J. T. 1985. Chondrules in the Qingzhen type 3 enstatite chondrite: Possible precursor components and comparison to ordinary chondrite chondrules. *Geochimica et Cosmochimica Acta* 49:1781–1795.

Grossman J. N., Alexander C. M. O'D., Wang J., and Brearley A. J. 2002. Zoned chondrules in Semarkona: Evidence for high- and low-temperature processing. *Meteoritics & Planetary Science* 37:49–74.

Grossman L. 1975. Petrology and mineral chemistry of Ca-rich inclusions in the Allende meteorite. *Geochimica et Cosmochimica Acta* 39:433–454.

GSECARS. 2007. CARS software developments, http://cars9.uchicago.edu/software/idl. Accessed 15 April 2007.

Hertz J., Ebel D. S., and Weisberg M. K. 2003. Tomographic study of shapes and metal abundances of Renazzo chondrules (abstract #1059). 34th Lunar and Planetary Science Conference. CD-ROM.

Heymann D., Smith M. J., and Anderson J. B. 1985. X-radiography of slabs of the Allende meteorite. *Meteoritics* 20:559–569.

Hounsfield G. N. 1980. Computed medical imaging. *Science* 210:22–28.

Hutchison R. and Bevan A. W. R. 1983. Conditions and time of chondrule accretion. In *Chondrules and their origins*, edited by King E. A. Houston: Lunar and Planetary Institute. pp. 162–179.

Hutchison R., Bevan A. W. R., Agrell S. O., and Ashworth J. R. 1979. Accretion temperature of the Tieschitz, H3, chondritic meteorite. *Nature* 280:116–119.

Hylton S. N., Ebel D. S., and Weisberg M. K. 2005. A 3-D tomographic survey of compound chondrules in CR chondrites (abstract #5305). *Meteoritics & Planetary Science* 40:A71.

Ignatyev K., Huwig K., Harvey R., Ishii H., Bradley J., Luening K., Brennan S., and Pianetta P. 2007. First X-ray fluorescence MicroCT results from micrometeorites at SSRL. Proceedings, Ninth International Conference on Synchrotron Radiation Instrumentation. pp. 1337–1340.

Ikeda S., Nakano T., Tsuchiyama A., Uesugi K., Suzuki Y., Nakamura K., Nakashima Y., and Yoshida H. 2004. Nondestructive three-dimensional element-concentration mapping of a Cs-doped partially molten granite by X-ray computed tomography using synchrotron radiation. *American Mineralogist* 89:1304–1313.

ImageJ. 2007. NIH Image home page. http://rsb.info.nih.gov/nih-image. Accessed 15 April 2007. See also http://www.scioncorp.com. Accessed 15 April 2007.

Imaris. 2007. Bitplane AG, Zürich, Switzerland. http://www.imaris.com. Accessed 15 April 2007.

Joung M. K. R., MacLow M.-M., and Ebel D. S. 2004. Chondrule formation and protoplanetary disk heating by current sheets in non-ideal magnetohydrodynamic turbulence. *The Astrophysical Journal* 606:532–541.

Ketcham R. A. and Carlson W. D. 2001. Acquisition, optimization, and interpretation of X-ray computed tomographic imagery: Applications to the geosciences. *Computers and Geosciences* 27: 381–400.

Ketcham R. A. and Iturrino G. J. 2005. Nondestructive high-resolution visualization and measurement of anisotropic effective porosity in complex lithologies using high-resolution X-ray computed tomography. *Journal of Hydrology* 302:92–106.

King T. V. V. and King E. A. 1978. Grain size and petrography of C2 and C3 carbonaceous chondrites. *Meteoritics* 13:47–72.

King T. V. V. and King E. A. 1979. Size frequency distribution of fluid drop chondrules in ordinary chondrules. *Meteoritics* 14:91–96.

Kitamura M., Tsuchiyama A., Uesugi K., and Nakano T. 2001. Three-dimensional structures of metal-sulfides in a CO chondrite using X-ray CT. *Antarctic Meteorites* 16:58–60.

Kondo M., Tsuchiyama A., Hirai H., and Koishickawa A. 1997. High-resolution X-ray computed tomographic (CT) images of chondrites and a chondrule. *Antarctic Meteorite Research* 10: 437–447.

Kornacki A. S., Cohen R. E., and Wood J. A. 1983. Petrography and classification of refractory inclusions in the Allende C3(V) chondrites. Proceedings of the Eighth Symposium on Antarctic Meteorites. pp. 45–60.

Krot A. N., Hutcheon I. D., and Keil K. 2002. Plagioclase-rich chondrules in the reduced CV chondrites: Evidence for complex formation history and genetic links between calcium-aluminum-rich inclusions and ferromagnesian chondrules. *Meteoritics & Planetary Science* 37:155–182.

Kuebler K. E., McSween H. Y., Jr., Carlson W. D., and Hirsch D. 1999. Sizes and masses of chondrules and metal-troilite grains in ordinary chondrites: Possible implications for nebular sorting. *Icarus* 141:96–106.

Kurat G., Zinner E., and Brandstätter F. 2002. A plagioclase-olivine-spinel-magnetite inclusion from Maralinga (CK): Evidence for sequential condensation and solid-gas exchange. *Geochimica et Cosmochimica Acta* 66:2959–2979.

Lauretta D. S., Killgore M., Benoit P. H., Moore S., and Sears D. W. G. 2002. NWA 505: A new LL3.0 chondrite with evidence for chondrule formation in a dust-rich environment (abstract #5069). *Meteoritics & Planetary Science* 37:A84.

Lentz R. C. F. and McSween H. Y., Jr. 2000. Crystallization of the basaltic shergottites: Insights from crystal size distribution (CSD) analysis of pyroxenes. *Meteoritics & Planetary Science* 35:919–927.

Maisey J. G. 2005. Braincase of the Upper Devonian shark Cladoides wildungensis (Chondrichthyes, Elasmobranchii) with observations on the braincase in early chondrichthyans. *Bulletin of the American Museum of Natural History* 288:1–103.

Martin P. M., Mills A. A., and Walker E. 1975. Preferential orientation in four C3 chondritic meteorites. *Nature* 257:37–38.

May C., Russell S. S., and Grady M. M. 1999. Analysis of chondrule and CAI size and abundance in CO3 and CV3 chondrites: A preliminary study (abstract #1688). 30th Lunar and Planetary Science Conference. CD-ROM.

McCoy T. J. and Carlson W. D. 1998. Opaque minerals in the GRA 95209 lodranite: A snapshot of metal segregation (abstract #1675). 29th Lunar and Planetary Science Conference. CD-ROM.

McCoy T. J., Taylor G. J., and Keil K. 1992. Zagami: Product of a two-stage magmatic history. *Geochimica et Cosmochimica Acta* 56:3571–3582.

McCoy T. J., Ketcham R. A., Benedix G. K., Carlson W. D., and Wilson L. 2002. Vesicular basalts from asteroids: Clues to physical process in their parent magmas (abstract #1213). 33rd Lunar and Planetary Science Conference. CD-ROM.

McCoy T. J., Wilson L., Benedix G. K., Ketcham R. A., Wadhwa M., and Davis A. M. 2003. Vesicular eucrites: Where and how did they form and why are they so rare (abstract #1187)? 34th Lunar and Planetary Science Conference. CD-ROM.

McSween H. Y., Jr. 1977. Chemical and petrographic constraints on the origin of chondrules and inclusions in carbonaceous chondrites. *Geochimica et Cosmochimica Acta* 41:1843–1860.

Mees R., Swennen R., van Geet M., and Jacobs P. 2003. Applications of X-ray computed tomography in the geosciences. In *Applications of X-ray computed tomography in the geosciences*, edited by Mees R., Swennen R., van Geet M., and Jacobs P. Geological Society Special Publication #215. London: The Geological Society of London. 243 p. (+CD).

Murray J., Boesenberg J. S., and Ebel D. S. 2003. Unambiguous voids in Allende chondrules and refractory inclusions (abstract #1999). 35th Lunar and Planetary Science Conference. CD-ROM.

Nakamura T., Tsuchiyama A., Akaki T., Uesugi K., Nakano T., and Noguchi T. 2007. Bulk mineralogy and three-dimensional tomography of individual Stardust particles (abstract #1107). 38th Lunar and Planetary Science Conference. CD-ROM.

NCAR. 2007. NetCDF (network Common Data Form) library page. http://www.unidata.ucar.edu/packages/netcdf. Accessed 15 April 2007.

Nettles J. W., Lofgren G. E., Carlson W. D., and McSween H. Y., Jr. 2003. An evaluation of quantitative methods of determining the degree of melting experienced by a chondrule (abstract #2004). 35th Lunar and Planetary Science Conference. CD-ROM.

Newton T. H. and Potts D. G. 1981. Technical aspects of computed tomography. In *Radiology of the skull and brain,* vol. 5. Saint Louis, Missouri: C.V. Mosby Co. pp. 3853–4419.

Okazawa T., Tsuchiyama A., Yano H., Noguchi T., Ozawa T., Nakano T., and Uesugi K. 2002. Measurement of densities of Antarctic micrometeorites using X-ray microtomography. Proceedings, 27th Symposium on Antarctic Meteorites. pp. 137–139.

Patzer A., Hill D. H., and Boynton W. V. 2001. Itqiy: A metal-rich enstatite meteorite with achondritic texture. *Meteoritics & Planetary Science* 36:1495–1505.

Prinz M., Weisberg M. K., Nehru C. E., and Delaney J. S. 1985. Chondrules of the Renazzo and Al Rais carbonaceous chondrites: Layering and accretionary growth as part of the chondrule-forming process (abstract #1073). Proceedings, 16th Lunar and Planetary Science Conference. pp. 677–678.

Proussevitch A. A. and Sahagian D. L. 2001. Recognition and separation of discrete objects within complex 3-D voxelized structures. *Computers and Geosciences* 27:441–454.

Richter F. M., Davis A. M., and Mendybaev R. A. 2002. How the type B1 CAIs got their melilite mantles (abstract #1901). 33rd Lunar and Planetary Science Conference. CD-ROM.

Rivers M. L. 2007. Tutorial introduction to X-ray computed microtomography data processing. http://www-fp.mcs.anl.gov/xray-cmt/rivers/tutorial.html. Accessed 15 April 2007.

Rivers M. L., Sutton S. R., and Eng P. 1999. Geoscience applications of X-ray computed microtomography. Proceedings, SPIE, Developments in X-ray tomography II, vol. 3772. pp. 78–86.

Rivers M. L., Sutton S. R., and Newville M. 2001. 3-D elemental mapping by synchrotron computed microtomography (abstract #3808). Eleventh Annual V. M. Goldschmidt Conference. CD-ROM.

RSI. 2007. Interactive Data Language, Research Systems International, ITT Industries. http://rsinc.com. Accessed 15 April 2007.

Rubin A. and Grossman J. N. 1987. Size-frequency distributions of EH3 chondrules. *Meteoritics* 22:237–251.

Rubin A. and Keil K. 1984. Size distributions of chondrule types in the Inman and Allan Hills A77011 L3 chondrites. *Meteoritics* 19: 135–142.

Sahagian D. L., Proussevitch A. A., and Carlson W. D. 2002. Analysis of vesicular basalts and lava emplacement processes for application as a paleobarometer/paleoaltimeter. *Journal of Geology* 110:671–685.

Schoenbeck T. S. and Ebel D. S. 2003. 3-D microtomographic determination of chondrule/matrix ratios in carbonaceous chondrites (abstract). *Geochimica et Cosmochimica Acta* 68: A765.

Seeram E. 2001. Computed tomography: Physical principles, clinical applications, and quality control, 2nd ed. Philadelphia: W.B. Saunders. 430 p.

Simon S. B., Grossman L., Krot A. N., and Ulyanov A. A. 2002. Bulk chemical compositions of type B refractory inclusions (abstract #1620). 33rd Lunar and Planetary Science Conference. CD-ROM.

Song S.-R., Jones K. W., Lindquist W. B., Dows B. A., and Sahagian D. L. 2001. Synchrotron X-ray computed microtomography: Studies on vesiculated basaltic rocks. *Bulletin of Volcanology* 63: 252–263.

Sorby H. C. 1877. On the structure and origin of meteorites. *Nature* 15:495–498.

SPring8. 2007. About SPring-8, Japan Synchrotron Radiation Research Institute. http://www.spring8.or.jp. Accessed 15 April 2007.

Srinivasan G., Huss G. R., and Wasserburg G. J. 2000. A petrographic, chemical, and isotopic study of calcium-aluminum-rich inclusions and aluminum-rich chondrules from the Axtell (CV3) chondrite. *Meteoritics & Planetary Science* 35: 1333–1354.

Stolper E. and McSween H. Y., Jr. 1979. Petrology and origin of the shergottite meteorites. *Geochimica et Cosmochimica Acta* 43: 1475–1498.

Sutton S. R. 2006. User research facilities in the earth sciences. *Elements* 2:7–8.

Tsuchiyama A., Kawabata T., McKay G. A., and Lofgren G. E. 1999. Three-dimensional structure of Martian meteorite ALH 84001 by X-ray CT method (abstract #1539). 30th Lunar and Planetary Science Conference. CD-ROM.

Tsuchiyama A., Kawabata T., Kondo M., Uesugi K., Nakano T., Suzuki Y., Yagi M., Umetani K., and Shirono S. 2000. Spinning chondrules deduced from their three-dimensional structures by X-ray CT method (abstract #1566). 31st Lunar and Planetary Science Conference. CD-ROM.

Tsuchiyama A., Uesugi K., Nakano T., Suzuki Y., and Yagi N. 2001. X-ray microtomography system using SR at SPring-8 for studies of three-dimensional microstructures of meteorites. *Antarctic Meteorites* 16:151–153.

Tsuchiyama A., Nakamura T, Nakano T., and Nakamura N. 2002. Three-dimensional description of the Kobe meteorite by micro X-ray CT method: Possibility of three-dimensional curation of meteorite samples. *Geochemical Journal* 36:369–390.

Tsuchiyama A., Uesugi K., Nakano T., and Ikeda S. 2005. Quantitative evaluation of attenuation contrast of X-ray computed tomography images using monochromatized beams. *American Mineralogist* 90:132–142.

Uesugi K., Suzuki Y., Yagi N., Tsuchiyama A., and Nakano T. 2001. Development of high spatial resolution X-ray CT system at BL47XU in SPring-8. *Nuclear Instruments and Methods in Physics Research* 467:853–856.

University of Texas. 2007. High-resolution X-ray CT facility. http://www.ctlab.geo.utexas.edu. Accessed 6 June 2006.

Van Geet M. and Swennen R. 2001. Quantitative 3-D fracture analysis by means of microfocus X-ray computer tomography (mu CT): An example from coal. *Geophysical Research Letters* 28:3333–3336.

Wadhwa M. 2001. Redox state of Mars' upper mantle and crust from Eu anomalies in shergottite pyroxenes. *Science* 291:1527–1530.

Wark D. A. and Lovering J. F. 1977. Marker events in the early evolution of the solar system: Evidence from rims on Ca-Al-rich inclusions in carbonaceous chondrites. 8th Lunar Science Conference. pp. 95–112.

Wasson J. T., Krot A. N., Lee M. S., and Rubin A. E. 1995. Compound chondrules. *Geochimica et Cosmochimica Acta* 59: 1847–1869.

Weisberg M. K., Prinz M., Clayton R. N., and Mayeda T. K. 1993. The CR (Renazzo-type) carbonaceous chondrite group and its implications. *Geochimica et Cosmochimica Acta* 57:1567–1586.

Weisberg M. K., Ebel D. S., Connolly H. C., Jr., Boesenberg J. S., and Castellano D. 2002. Petrologic-tomographic study of metal in the CR chondrites (abstract #5254). *Meteoritics & Planetary Science* 37:A149.

Weitz C. M., Rutherford M. J., and Head J. W. 1997. Oxidation states and ascent history of the Apollo 17 volcanic beads as inferred from metal-glass equilibria. *Geochimica et Cosmochimica Acta* 61:2765–2775.

Weitz C. M., Rutherford M. J., Head J. W. III, and McKay D. S. 1999. Ascent and eruption of a lunar high-titanium magma as inferred from the petrology of the 75001/2 drill core. *Meteoritics & Planetary Science* 34:527–540.

Wildenschild D., Vaz C. M. P., Hopmans J. W., Rivers M. L., Rikard D., and Ruddle D. G. 2000. Imaging of multi-phase flow processes and phase distributions at various scales using X-ray tomography. *Eos* 81:F432–F433.

Wildenschild D., Simunek J., and Hopmans J. W. 2001. Flow rate dependence of soil hydraulic characteristics. *Soil Science Society of America Journal* 65:35–48.

Woronow A. and King E. A. 1985. Chondrule volume percents: Statistical behavior and visual-estimation guides produced by numerical simulation. *Meteoritics* 20:103–112.

Zega T. J., Garvie L. A. J., Dódony I., Friedrich H., Stroud R. M., and Buseck P. R. 2006. Polyhedral serpentine grains in CM chondrites. *Meteoritics & Planetary Science* 41:681–688.

Zieg M. J., and Lofgren G. E. 2003. Crystal size distributions from porphyritic olivine chondrules: Insights into formation conditions (abstract #1384). 34th Lunar and Planetary Science Conference. CD-ROM.